J. Fluid Mech. (2006), *vol.* 551, *pp.* 235–274.
doi:10.1017/S0022112005008463 Printed in the United Kingdom

Kelvin waves and the singular modes of the Lamb–Oseen vortex

By DAVID FABRE[1,2], DENIS SIPP[2] AND LAURENT JACQUIN[2]

[1]IMFT, Allée du Professeur Camille Soula, 31400 Toulouse, France

[2]ONERA, Fundamental and Experimental Aerodynamics department, 8 rue des Vertugadins, 92190 Meudon, France

(Received 20 September 2004 and in revised from 7 September 2005)

Columnar vortices are known to support a family of waves initially discovered by Lord Kelvin (1880) in the case of the Rankine vortex model. This paper presents an exhaustive cartography of the eigenmodes of a more realistic vortex model, the Lamb–Oseen vortex. Some modes are Kelvin waves related to those existing in the Rankine vortex, while some others are singular damped modes with a completely different nature. Several families are identified and are successively described. For each family, the underlying physical mechanism is explained, and the effect of viscosity is detailed. In the axisymmetric case (with azimuthal wavenumber $m = 0$), all modes are Kelvin waves and weakly affected by viscosity. For helical modes ($m = 1$), four families are identified. The first family, denoted D, corresponds to a particular wave called the displacement wave. The modes of the second family, denoted C, are cograde waves, except in the long-wave range where they become centre modes and are strongly affected by viscosity. The modes of the third family, denoted V, are retrograde, singular modes which are always strongly damped and do not exist in the inviscid limit. The modes of the last family, denoted L, are regular, counter-rotating waves for short wavelengths, but they become singular damped modes for long wavelengths. In an intermediate range of wavelengths between these two limits, they display a particular structure, with both a wave-like profile within the vortex core and a spiral structure at its periphery. This kind of mode is called a critical layer wave, and its significance is explained from both a physical and a mathematical point of view. Double-helix modes ($m = 2$) can similarly be classified into the C, V and L families. One additional mode, called F, plays a particular role. For short wavelenghs, this mode corresponds to a helical flattening wave, and has a clear physical significance. However, for long wavelenghts, this mode completely changes its structure, and becomes a critical layer wave. Modes with larger azimuthal wavenumbers m are all found to be substantially damped.

1. Introduction

1.1. *Historical background*

In a celebrated paper dated 1880, Lord Kelvin (previously known as Sir W. Thomson, before he received a peerage in 1892) examined the vibrations of a columnar vortex. After deriving the equations describing the evolution of disturbances on a vortex in the general case, he examined several particular cases and gave analytical predictions concerning the vibration frequencies. One of these particular cases corresponded to

a "core of uniform vorticity (that is to say, rotating like a solid), surrounded by irrotationally rotating liquid with no slip at the interface". In modern terms, this vortex model is known as the Rankine vortex, and the waves sustained by it are called 'Kelvin vortex waves' (or more simply Kelvin waves when no confusion with the 'Kelvin tidal waves' occurring in geophysics is possible). The solution of Kelvin (1880) still forms the basis of most studies on vortex waves and is reproduced in several textbooks (e.g. Saffman 1992; Rossi 2000).

The motivation which led Lord Kelvin to study vortex dynamics is quite interesting from a historical point of view, and is explained in a 1867 paper entitled 'On vortex atoms'. Quoting Lord Kelvin (1867), "Helmholtz's admirable discovery of the law of vortex motion [...] inevitably suggests that Helmholtz's rings are the only true atoms". This argument is developed as follows: "Helmholtz has provided an absolutely inalterable quality in the motion of any portion of a perfect fluid in which the peculiar motion which he calls 'Wirbelbewegung' (i.e., vorticity) has once been created. Thus any portion of a perfect fluid which has 'Wirbelbewegung' has one of recommendation of Lucretus's atoms – infinitely perennial specific quality".

Lord Kelvin thus proposed founding a theory based on "the hypothesis that all bodies are composed of vortex atoms in a perfect homogeneous fluid". According to this theory, each atom specie was to be associated to a particular knitted or knotted vortex structure, "the variety of which [being] infinitely more than sufficient to explain the varieties and allotropies of known simple bodies and their mutual affinities". Moreover, the modes of vibration of those vortex structures were expected to explain the recently discovered spectral emission phenomenon. For example, the double frequency of the yellow sodium light would be explained by a structure for the sodium vortex atom admitting two fundamental modes of vibration. Still quoting Lord Kelvin, "It seems [...] probable that the sodium atom may not consist of a single vortex line, but it may very probably consist of two approximately equal vortex rings passing through each other like two links in a chain". In that context, the 1880 article on the 'Vibrations of a columnar vortex', which was announced in the 1867 paper but was only to appear thirteen years later, was presented as one of the first elementary steps towards this new theory.

The theory of vortex atoms may seem somewhat esoteric to a modern observor, but at that time it was favourably accepted as a working hypothesis by a large part of the scientific community. It must be recalled that several decades were to pass until the historical discovery of the atomic structure by Rutherford (1911). Since then the theory of vortex atoms has not been defended seriously by anyone. However, it is fascinating to note that Lord Kelvin's original ideas survive in at least two domains of modern research. First, the efforts to classify knots according to their topological properties, first expected to give a basis for the classification of atoms, gave birth to the mathematical theory of knots. This theory is currently flourishing and has found modern applications in the field of cryptography. Secondly, the most exciting theory of fundamental particles at the present time, string theory, has a definite resemblance to vortex atoms.

1.2. *Review of recent work*

The problem initially considered by Lord Kelvin still has a variety of applications. For example, an application which motivated much work in the last three decades is the dynamics of trailing vortices shed by the wings of transport aircraft. Here, the vortices are harmful because of the danger they represent to following aircraft, and instabilities resulting from the coupling between Kelvin waves are thought of as a possible way to alleviate them (see Spalart 1998; Jacquin *et al.* 2003). Another application is the

dynamics of coherent vortical structures which are ubiquous in turbulent fields and play a key role in the transport of momentum and the dissipation. Yet another application is the dynamics of tornadoes.

A large amount of work has been devoted to vortex stability in the last thirty years. Recent reviews on the topic can be found in Ash & Khorrami (1995), Rossi (2000), and in the context of aircraft trailing wakes, in Jacquin *et al.* (2003). In recent literature, effort is mainly directed at identifying and describing vortex instabilities. Two main kinds of instabilities have received particular interest. The first kind occur in the presence of a core axial flow within the vortex. Several families of such instabilities, both inviscid and viscous, have been identified and described (see Mayer & Powell 1992; Fabre & Jacquin 2004*b*; and references therein). The second kind of instabilities occur in vortex systems. They are called cooperative instabilities, and are due to the straining field induced on each vortex by the others. Cooperative instabilities can be classified into long-wave and short-wave ones. The long-wave cooperative instabilities were discovered by Crow (1970) in the case of a vortex pair, and were generalized to the case of multiple vortex pairs by Crouch (1997) and Fabre, Jacquin & Loof (2002). The short-wave ones, which are related to the generic elliptic instability mechanism (Kerswell 2002), were discovered by Moore & Saffman (1975) and Tsai & Widnall (1976) and are the object of numerous recent studies (see Le Dizès & Laporte 2002; Sipp & Jacquin 2003; Fukumoto 2003; Fabre & Jacquin 2004*a*; and related papers). Note that both kinds of cooperative instabilities can be explained as a resonance mechanism involving a pair of Kelvin waves. Therefore, an inspection of these waves is necessary prior to an investigation of the instability.

Compared to this abundant literature devoted to vortex instabilities, Kelvin waves, which are at best neutral and generally damped, have received less interest. Only two kinds of waves have been investigated in the last few decades. First, axisymmetric waves have been studied by Benjamin (1962) and Leibovich (1970) (among others). The motivation for those studies came from the vortex breakdown phenomenon, which is related to a transition from a supercritical state (where axisymmetric waves only propagate downstream) to a subcritical state (where axisymmetric waves propagate both upstream and downstream).

Secondly, the particular helical wave referred to herein as the displacement wave, which is responsible for long-wave distortions of a vortex filament, plays a key role in at least three very different situations. First, in aircraft vortex wakes, it participates in the long-wave cooperative instability mechanism mentioned above (Crow 1970; Moore & Saffman 1972; Widnall, Bliss & Zalay 1971). Secondly, in rotating turbulence, it is responsible for the transport of momentum and energy from turbulent zones to quieter zones (Hopfinger, Browand & Gagne 1982). Finally, the propagation of Kelvin displacement waves along quantized vortices is essential to the transfer of energy in superfluid turbulence (Barenghi, Donelli & Wien 2001). Thus, this kind of wave has been studied extensively using various methods, such as asymptotic expansions of the stability equations (Leibovich, Brown & Patel 1986), or vortex filament methods (Samuels & Donelly 1990; Klein & Majda 1991*a*, *b*; and related papers).

In addition to the applications described above, recent developments indicate at least two situations where Kelvin waves seem to play a key role. First, Kelvin waves may be excited by a turbulent field surrounding the vortex core. This was shown using numerical simulations by Melander & Hussain (1993) and was further demonstrated for a Rankine vortex by Miyazaki & Hunt (2000) in the context of rapid distortion theory. Recently, Antkowiak & Brancher (2004) performed an optimal perturbation analysis of a Lamb–Oseen vortex and also observed that some kinds of helical

waves can be efficiently excited. This excitation of waves by surrounding turbulence is suspected to be responsible for the vortex meandering phenomenon, which is ubiquous in trailing vortex experiments (Jacquin *et al.* 2003). Secondly, a phenomenon called vortex bursting, which is known to occur in an unpredictable way on trailing vortices (Spalart 1998), seems to be explainable as resulting from the collision of two axisymmetric wave packets propagating in opposite directions (Moet *et al.* 2005).

Despite the ubiquous role of Kelvin waves in vortex dynamics, the only case which has been studied in a comprehensive way is the Rankine vortex initially considered by Lord Kelvin (1880). However, this model is somewhat unrealistic because of the discontinuity of the vorticity field at the vortex interface. Furthermore, it is by nature an inviscid model, and does not allow consideration of the effect of viscosity on the waves in a proper way. Therefore, the application of Lord Kelvin's results to real-life vortices is questionable, and more representative vortex models have to be considered. One of the simplest models for this purpose is the Lamb–Oseen vortex, defined by a Gaussian distribution of vorticity. Motivated by the application to short-wave cooperative instabilities, Sipp conducted a numerical stability study of this vortex model in the inviscid case (Sipp 1999; see also Sipp & Jacquin 2003). He discovered that in addition to regular, non-damped waves, the Lamb–Oseen vortex also possesses singular, damped modes. This feature is a significant qualitative difference with the case of a Rankine vortex where all waves are strictly neutral. The results of Sipp were recently complemented by Le Dizès & Lacaze (2005) using a large-wavenumber asymptotic analysis.

The computation of inviscid singular modes such as those previously described requires a deformation of the integration path into the complex r-plane. This procedure, which is commonly used for the stability of parallel flows, leads to the prediction of modes possessing a critical layer singularity. This singularity must be regularized using either viscosity or nonlinearity. Le Dizès (2004) recently justified this procedure in the viscous case using a large-Reynolds-number asymptotic analysis. His results indicate that the inviscid modes computed by Sipp may effectively be reached as the limit of modes computed in the viscous framework as $Re \to \infty$. In addition, he described the structure of these modes in the vicinity of the critical layer. It is one of the objectives of the present paper to check these predictions.

In a related study (Fabre 2002) the linear dynamics of the Lamb–Oseen vortex is investigated from the complementary point of view of an initial value problem. Several kinds of initially localized perturbations are imposed on the vortex and give rise to the propagation of wave packets. The results are compared to a similar study performed by Arendt, Fritts & Andreassen (1997) for the Rankine vortex and important differences are pointed out. That study complements the present one and illustrates how the various waves presented here can effectively contribute to the response of a vortex to a localized perturbation.

1.3. *Presentation of the paper*

This paper has three goals. The first is to provide an exhaustive description of the normal modes of the Lamb–Oseen vortex, and to propose a complete classification of the modes into several families. To achieve this, the various families of modes are successively described and their structure is illustrated, focusing on a moderate value of the Reynolds number ($Re = 1000$), and on the long and medium wavelength range (i.e. wavelengths comparable to the core radius and longer).

The second goal is to clarify the physical mechanisms responsible for wave propagation. The occurrence of waves is usually attributed to the rotation of the

vortex core, and Kelvin waves are thought of as inertial waves due to rotation which are guided along the vortex core (Rossi 2000). This picture is accurate when considering waves with short wavelengths compared to the vortex core. For example, in the short-wave limit, the relative frequency of the waves (with respect to the frame rotating with the vortex centre) is, in absolute value, twice the background rotation rate (Le Dizès & Lacaze 2005), just the value corresponding to pure inertial waves. On the other hand, this picture is questionable in the long and medium wavelength regimes. As will be shown, different underlying physical mechanisms have to be invoked for each family of waves.

The third goal is to investigate the effect of viscosity. First, viscosity is found to lead to a new class of fully viscous, strongly damped modes, which coexist with the Kelvin waves. Secondly, and most interestingly, the effect of viscosity is found to be singular for most of the Kelvin waves, in the sense that the corresponding eigenmodes do not possess a regular limit as $Re \to \infty$. Two main kinds of singularities are described. The first is a critical layer singularity. In this case, the modes are inviscid at leading order except in an annular region outside the vortex where viscosity occurs at leading order and leads to the appearance of a spiral structure. For these modes, comparisons with the inviscid results of Sipp & Jacquin (2003), and with the asymptotic analyses of Le Dizès (2004) and Le Dizès & Lacaze (2005) will be presented. The second kind of singularity, which occurs for most waves in the long-wave limit, is a centre-mode singularity. In this case the radial structure of the modes shrinks towards the vortex centreline, leading to an enhanced dissipation.

The paper is organized as follows. Section 2 presents the base flow, the stability equations and the numerical method. Section 3 introduces the nomenclature used for the classification of the normal modes into several families. The axisymmetric modes ($m = 0$) are presented in § 4. The study of helical modes ($|m| = 1$), presented in § 5, forms the largest part of this paper. Four families of modes, called D, C, V and L, are identified and successively described (in §§ 5.1, 5.2, 5.3 and 5.4). Section 6 considers the cases of double-helix modes ($|m| = 2$) and higher-order modes. Section 7 summarizes the conclusions.

2. Starting equations and numerical method

2.1. *Base flow*

The base flow considered in this paper is a Lamb–Oseen vortex, oriented along the z-direction, with a circulation Γ and a radius a, in an incompressible fluid of density $\rho = 1$ and viscosity ν. The geometry and the coordinate system are sketched in figure 1. Note that the z-axis is directed in the horizontal direction, so that the direction of negative and positive z will simply be referred to as the 'left' and 'right' directions.

Using cylindrical coordinates (r, θ, z), the azimuthal velocity law of the Lamb–Oseen vortex is

$$V(r) = \frac{\Gamma}{2\pi r}\left(1 - \mathrm{e}^{-r^2/a^2}\right). \tag{2.1}$$

This model corresponds to a self-similar solution of the Navier–Stokes equation with a radius increasing in time as $a(t)^2 = a(0)^2 + 4\nu t$. Here, the base-flow diffusion is ignored and the vortex is considered as 'frozen', with a constant radius a. The effect of viscosity is characterized by a Reynolds number, defined as $Re = \Gamma/(2\pi\nu)$. For non-dimensionalization, the vortex radius is taken as $a = 1$, and the circulation as $\Gamma = 2\pi$. In the following, $\Omega(r) = V(r)/r = (1 - \mathrm{e}^{-r^2})/r^2$ and $\Xi(r) = (1/r)(\partial/\partial r)[rV(r)] = 2e^{-r^2}$ will denote, respectively, the angular velocity and the axial vorticity.

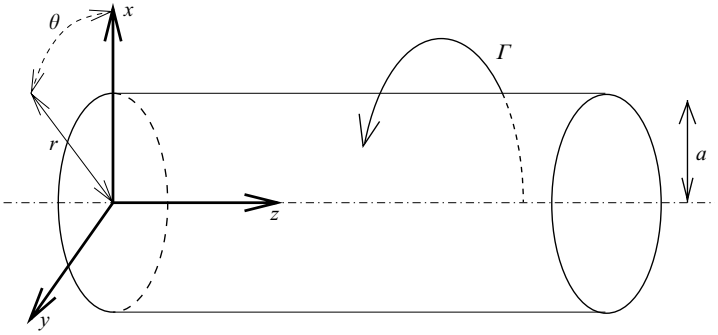

FIGURE 1. Sketch of the vortex and coordinate systems.

The approximation of a frozen base flow is commonly done in stability analyses because it allows perturbations to be considerd in the form of eigenmodes. However, on the time scale $t = O(Re)$ where the base-flow diffusion becomes non-negligible, eigenmodes cease to be a valid approximation of the solution. As a consequence, it must be kept in mind that an eigenmode is only relevant when its own time scale (the inverse of its frequency or the inverse of its damping rate, depending on which quantity is most relevant) is smaller than Re.

2.2. *Stability equations*

In the stability analysis we consider infinitesimal disturbances in the form of eigenmodes, characterized by an axial wavenumber k, an azimuthal wavenumber m, and a complex frequency ω, i.e.

$$(u'_r, u'_\theta, u'_z, p') = [u(r), v(r), w(r), p(r)] \exp(\mathrm{i}kz + \mathrm{i}m\theta - \mathrm{i}\omega t) + \text{c.c.}, \tag{2.2}$$

where c.c. stands for the complex conjugate. Linearization of the continuity, r-, θ- and z-momentum equations leads to the following set of equations:

$$\frac{1}{r}\frac{\partial}{\partial r}(ru) + \frac{\mathrm{i}m}{r}v + \mathrm{i}kw = 0, \tag{2.3a}$$

$$\mathrm{i}(m\Omega - \omega)u - 2\Omega v + \frac{\partial p}{\partial r} = \frac{1}{Re}\left[\left(\Delta_{m,k} - \frac{1}{r^2}\right)u - \frac{2\mathrm{i}m}{r^2}v\right], \tag{2.3b}$$

$$\mathrm{i}(m\Omega - \omega)v + \Xi u + \frac{\mathrm{i}m}{r}p = \frac{1}{Re}\left[\left(\Delta_{m,k} - \frac{1}{r^2}\right)v + \frac{2\mathrm{i}m}{r^2}u\right], \tag{2.3c}$$

$$\mathrm{i}(m\Omega - \omega)w + \mathrm{i}kp = \frac{1}{Re}\Delta_{m,k}w. \tag{2.3d}$$

In these equations, the notation $\Delta_{m,k}$ corresponds to the Laplacian operator, i.e.

$$\Delta_{m,k} = \frac{\partial^2}{\partial r^2} + \frac{1}{r}\frac{\partial}{\partial r} - k^2 - \frac{m^2}{r^2}. \tag{2.4}$$

When proper limit conditions are imposed (see, for example, Fabre & Jacquin 2004*b*), this system constitutes an eigenvalue problem which admits non-trivial solutions for discrete sets of (ω, m, k). In this paper we perform a temporal stability analysis, which consists of setting the wavenumbers (m, k) with k real and solving for the frequency ω, which is *a priori* a complex number. The real part of the frequency ω_r is the oscillation rate of the wave, and the imaginary part ω_i, which is always negative here, corresponds to its damping rate.

In the description of the eigenmodes, we will often refer to the radial, azimuthal, and axial components of the vorticity, defined as follows:

$$\xi_r = \frac{\mathrm{i}mw}{r} - \mathrm{i}kv, \quad \xi_\theta = \mathrm{i}ku - \frac{\partial w}{\partial r}, \quad \xi_z = \frac{1}{r}\frac{\partial (rv)}{\partial r} - \frac{\mathrm{i}mu}{r}. \tag{2.5}$$

2.3. *Numerical method*

The numerical method used here is a Chebyshev spectral collocation method, essentially identical to that described in Fabre & Jacquin (2004*b*) and Fabre (2002). This method consists of the following steps:

(i) The stability equations (2.3$a-d$) are manipulated in order to eliminate the pressure and axial velocity components. This leads to a reduced system for $[u(r), v(r)]^T$.

(ii) This reduced system is mapped from the physical domain $r \in [-\infty, \infty]$ to the Chebyshev domain $\xi \in [-1, 1]$. Here, two mapping functions are used. The first one is the algebraic mapping used in Fabre & Jacquin (2004*b*), and the second one is a complex mapping which is presented in Appendix B.

(iii) The unknown eigenfunctions $u(\xi)$ and $v(\xi)$ are expanded as a series of $N+1$ Chebyshev polynomials in terms of the mapped variable ξ. Thanks to the parity properties of the eigenfunctions, only odd polynomials are used for even wavenumbers m, and only even polynomials are used for odd wavenumbers m.

(iv) The Chebyshev expansions are introduced into the stability equations, which are expressed at $N+1$ suitably defined collocations points. This leads to a discretized eigenvalue problem with order $2(N+1)$.

(v) This discretized eigenvalue problem is solved using a global eigenvalue method. Here, this is done with the QZ algorithm, as implemented in the LAPACK routine ZGGEV.

(vi) Finally, the physically relevant modes are sorted from the spurious ones using a suitably defined convergence criterion.

As discussed in Fabre & Jacquin (2004*b*), this method is rapid and efficient, and allows accurate results without the need of an explicit imposition of the limit conditions. The number of collocation points of $N = 140$ was used in most of the computations. This value was found to be large enough to resolve accurately the spectrum of the Lamb–Oseen vortex, and low enough to guarantee the absence of round-off errors due to the stiffness of the eigenvalue problem.

The complex mapping was particularly helpful to compute the frequencies of the modes belonging to the L family (figures 6 and 20). On the other hand, all the figures displaying the structure of the modes had to be done using the real mapping.

3. Wave classification

This section introduces several definitions which are helpful in classifying the eigenmodes from a physical point of view.

The azimuthal wavenumber m allows the modes to be classified according to their geometry. The value $m = 0$ corresponds to *axisymmetric modes* or, following Saffman (1992), 'sausaging modes'. Eigenmodes with $m = \pm 1$ are *helical modes*, also called 'bending modes'. Eigenmodes with $|m| > 1$ are multiple helices, and Saffman (1992) proposed the name 'fluted modes'.

The quantity $-m/k$ corresponds to the pitch, and the sign of this quantity distinguishes *left-handed helices* ($m/k > 0$) from *right-handed helices* ($m/k < 0$). Due to the symmetries of the problem, $\omega(m, k) = \omega(m, -k) = -\omega^*(-m, k)$, the star denoting the

complex conjugate. So, left-handed and right-handed modes have symmetrical properties, and in the analysis we shall restrict to $m \geqslant 0, k \geqslant 0$ without loss of generality.

For $m \neq 0$, the quantity ω_r/m corresponds to the angular frequency of the mode. Modes such that $\omega_r/m \geqslant 1$ are observed to rotate faster than the vortex core and will be called *cograde modes*. Modes such that $0 \leqslant \omega_r/m \leqslant 1$ rotate in the same direction as the vortex, but when observed in a frame rotating with the vortex centreline they appear to rotate in the opposite direction. They will be referred to as *retrograde modes*. Modes with $\omega_r/m \leqslant 0$ are observed to rotate in a direction opposite to that of the vortex core, and will be referred to as *countergrade modes*. Finally, modes with $\omega_r = 0$ are *stationary modes*. The two latter categories only exist for $m = \pm 1$.

The quantity $\partial\omega_r/\partial k$ corresponds to the *group velocity*, and indicates the propagation velocity of wave packets in the axial direction. According to the conventions introduced in figure 1, modes with $\partial\omega_r/\partial k < 0$ and $\partial\omega_r/\partial k > 0$ will be referred to as *left-propagating modes* and *right-propagating modes*, respectively.

Note that some authors have distinguished *slow waves* and *fast waves* according to their phase velocity ω_r/k in the long-wave limit. However, this choice may lead to some inconsistencies and difficulties; for example, the phase velocity may be infinite for some waves, and does not respect Gallilean invariance. As a consequence, we did not follow this classification here and preferred to use the group velocity.

Finally, the asymptotic properties of the eigenmodes in the limit $Re \to \infty$ allow them to be classified into *regular modes* and *singular modes*. Eigenmodes are considered as regular when both their frequency and their eigenstructure admit a regular development with the following form:

$$\omega = \omega^{(0)} + Re^{-1}\omega^{(1)} + O(Re^{(-2)}), \tag{3.1}$$

$$[u(r), v(r), w(r), p(r)] = \boldsymbol{u}^{(0)}(r) + Re^{-1}\boldsymbol{u}^{(1)}(r) + O(Re^{(-2)}). \tag{3.2}$$

For such regular modes, the leading order $[\omega^{(0)}, \boldsymbol{u}^{(0)}(r)]$ can be computed using the inviscid equations, and the corresponding frequency $\omega^{(0)}$ is always pure real. The term $\omega^{(1)}$ is pure imaginary and gives the leading-order contribution to the damping rate. The term $\boldsymbol{u}^{(1)}(r)$ corresponds to the viscous correction to the eigenmode structure.

In the following, we will restrict the name *Kelvin waves* to the regular modes, because of their clear relation to the waves initially discovered by Lord Kelvin (1880) for the Rankine vortex. On the other hand, we will call the modes which do not follow this development 'singular modes' (although the two categories overlap, to a certain extent, in the case of the critical layer waves).

4. Axisymmetric modes ($m = 0$)

4.1. *Description*

We begin our presentation with the axisymmetric modes ($m = 0$). Figure 2 displays the oscillation rates ω_r computed for $Re = 1000$, in the range of axial wavenumbers $0 \leqslant k \leqslant 5$. In this figure, we have represented with a greyscale the damping rates ω_i. With this convention, the dark curves correspond to weakly damped waves, and the branches progressively lighten and vanish as their damping rate increases. Two sets of branches with symmetric frequencies can be distinguished. The waves of the first set have positive oscillation frequencies ω_r and positive slopes $\partial\omega_r/\partial k$ (i.e. group velocities), so they can be identified as *right-propagating waves*. The waves of the second set are *left-propagating waves* with negative oscillation frequencies ω_r and symmetrical properties. These features are essentially similar to the case of a Rankine

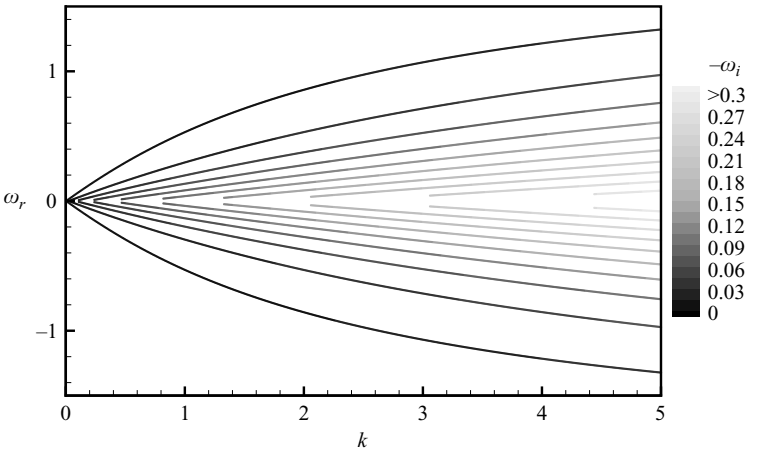

FIGURE 2. Frequencies of the axisymmetric ($m = 0$) eigenmodes, for $Re = 1000$.

vortex (e.g. Saffman 1922; Arendt *et al.* 1997), except, of course, for the damping rate resulting from viscosity.

Figure 3 illustrates the structure of some axisymmetric waves. The plots display iso-levels of the axial vorticity $\mathrm{Re}[\xi_z(r)\exp(\mathrm{i}kx)]$ (upper half) and the azimuthal vorticity $\mathrm{Re}[\xi_\theta(r)\exp(\mathrm{i}kx)]$ (lower half) of the eigenmodes in the (r, z)-plane. The four examples of waves depicted in the figure correspond to those computed for $k = 1$, on the first and second branches of right-propagating and left-propagating waves (numbered from outermost to innermost), respectively. As can be observed, the radial structure of the ξ_z eigencomponent displays one node for the waves computed on the first branches, and two nodes for those computed on the second branches (and so on for the higher branches). The left-propagating waves differ from their right-propagating counterparts by a phase shift between the ξ_z and ξ_θ components, and also, by a slight dissymmetry of their structure (which can be seen by comparing the position of the iso-level corresponding to the value 0 between plots *a* and *c*, or *b* and *d*). This latter effect is a result of viscosity: in the purely inviscid case the structure of the left-propagating and right-propagating waves would be identical.

Finally, it is worth mentioning that all the axisymmetric waves computed and presented here conserve the circulation of the vortex (because the limit conditions require the eigencomponents to decrease exponentially as $r \to \infty$, and therefore the associated circulation $2\pi r v(r)$ vanishes).

4.2. *Physical mechanism*

The physical mechanism responsible for the propagation of axisymmetric waves is explained in figure 4.

Figure 4(*a*) displays the structure of a vortex deformed by an axisymmetric standing wave†. The perturbed vortex has a varicose shape, which consists of an alternance of regions of high and low vorticity. Because of the conservation of circulation, the vortex radius is smaller in the regions of high vorticity and larger in the regions of low vorticity.

† What we call a standing wave is a perturbation oscillating in place without propagating. As in other well-known situations (for example, acoustic or surface waves), such a standing wave can be constructed as the superposition of two propagating waves with opposite directions.

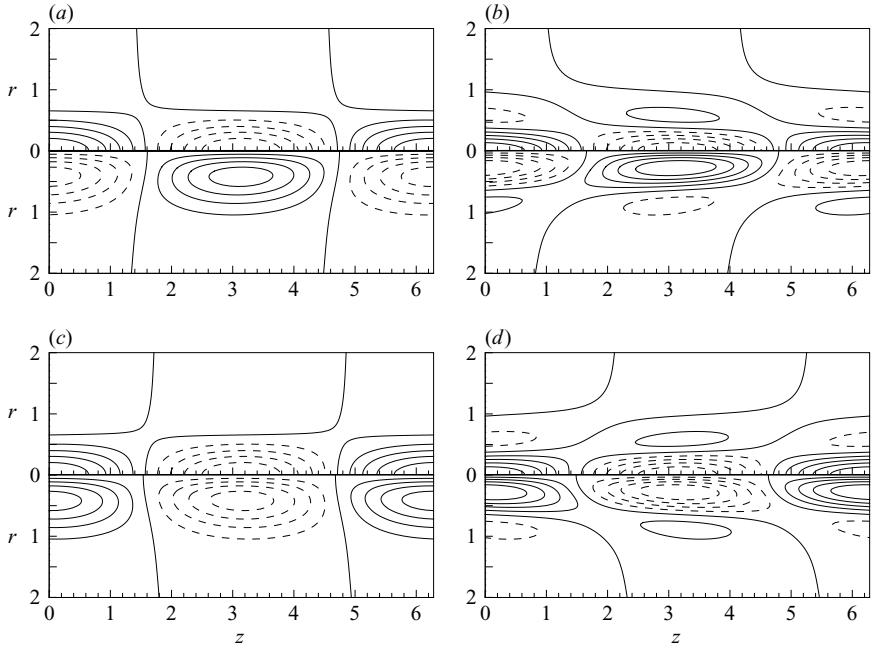

FIGURE 3. Structure of some axisymmetric Kelvin waves, for $Re = 1000$, $k = 1$: (a,b) first and second right-propagating waves; (c,d) first and second left-propagating waves. The upper and lower parts of the figure display, respectively, the axial vorticity (ξ_z) and azimuthal vorticity (ξ_θ) components in the (r,z)-plane. Nine equally spaced iso-levels are displayed (including zero), and the dashed levels correspond to negative values. (a) $\omega = 0.5306 - 0.0078\mathrm{i}$, (b) $\omega = 0.2973 - 0.0243\mathrm{i}$, (c) $\omega = -0.5306 - 0.0078\mathrm{i}$, (d) $\omega = -0.2973 - 0.0243\mathrm{i}$.

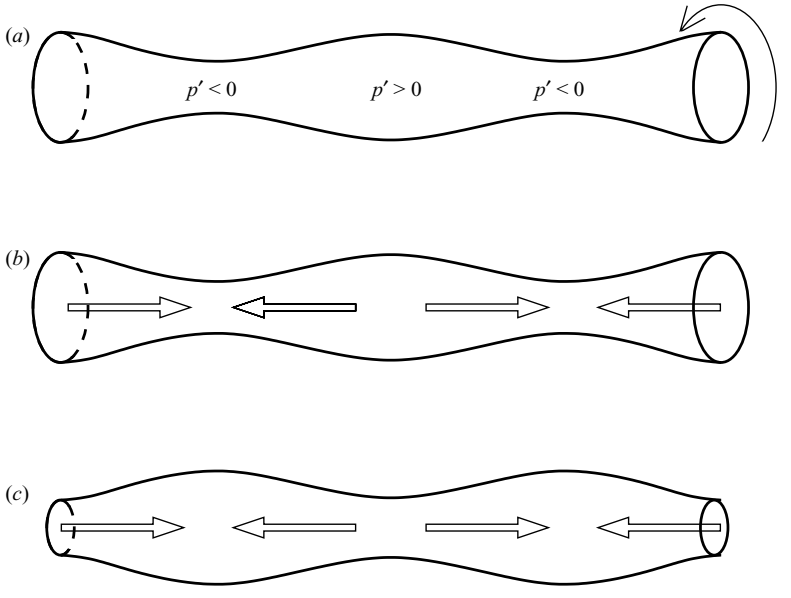

FIGURE 4. The physical mechanism for the propagation of axisymmetric Kelvin waves. See explanations in text.

Now, the thinner the vortex is, the larger is the depression within its core. Therefore, the varicose shape is associated with an alternance of high and low pressure perturbations (with respect to the pressure level of the vortex core in the unperturbed state). Therfore, a net axial pressure gradient exists within the core, and induces an axial flow. This effect is indicated by the arrows in figure 4(*b*).

Finally, as illustrated in figure 4(*c*), the axial flow within the vortex affects the axial vorticity through a stretching–compressing mechanism. In the regions of axial divergence, the vorticity is stretched, and the vortex radius is reduced. On the other hand, in the regions of axial convergence, the vorticity is compressed, and the vortex radius is augmented. The final effect is to reverse the initial varicose shape of the vortex. Note that an alternative explanation, based on the twisting of the vortex lines, was proposed by Melander & Hussain (1994) and Arendt *et al.* (1997).

The mechanism illustrated above strictly applies only to a standing wave, and only to the waves corresponding to the first branch, with the simplest internal structure (such as those depicted in figures 3(*a*) and 3(*c*)). However, a standing wave can be constructed as the superposition of a left-propagating wave and a right-propagating wave, and the mechanism for standing and propagating waves is the same, except for a phase shift between the ξ_z and w components. This sequence of events also applies to the waves on the higher branches, such as those described in figures 3(*b*) and 3(*d*), except that the mechanisms act in opposite directions in the inner and outer parts of the vortex.

4.3. *Effect of viscosity*

The effect of viscosity on the axisymmetric waves has been investigated by repeating the calculations with other values of the Reynolds number, and also by asymptotic analyses in the limit $Re \to \infty$ (Fabre 2002). This effect is quite trivial and only a brief account is given here. Axisymmetric waves are all found to be *regular* according to the definition given in § 3. On each branch, the leading-order frequency $\omega^{(0)}$ is pure real and corresponds to the inviscid frequency computed by Sipp & Jacquin (2003). The next term $\omega^{(1)}$ is pure imaginary and corresponds to the damping rate. This damping rate is a growing function of k, and for fixed k it is larger for the waves on the higher branches. These features are consistent with the greyscales of the curves in figure 2. The eigenmodes admit a regular development with the form (3.2), and the term $\boldsymbol{u}^{(1)}$ is responsible for the dissymmetry between left- and right-propagating waves which has been observed in figure 3.

Note, however, that the regular development (3.1)–(3.2) ceases to be valid in the long-wave limit ($k \to 0$). Inspection shows that this occurs as soon as $k = O(Re^{-1})$. However, this limit seems of little practical interest.

5. Helical modes ($m = 1$)

Figure 5 displays the frequencies of helical, left-handed ($m = 1$) modes computed for $Re = 1000$ (with the same conventions as in figure 2), and figure 6 shows a close-up view of these results for the range $0 < \omega_r < 0.16$. The picture is, at first sight, far more complex than for the axisymmetric case. At least four families of branches of the dispersion relation can be distinguished, and are identified by letters D, C, V and L in the figure.

The first family, called D, consists of the particular wave which is countergrade and left-propagating for all wavelengths, and whose frequency vanishes as $k \to 0$. The branches of the second family, called C, are right-propagating, cograde waves, except in the long-wave range where they become retrograde. The branches of the

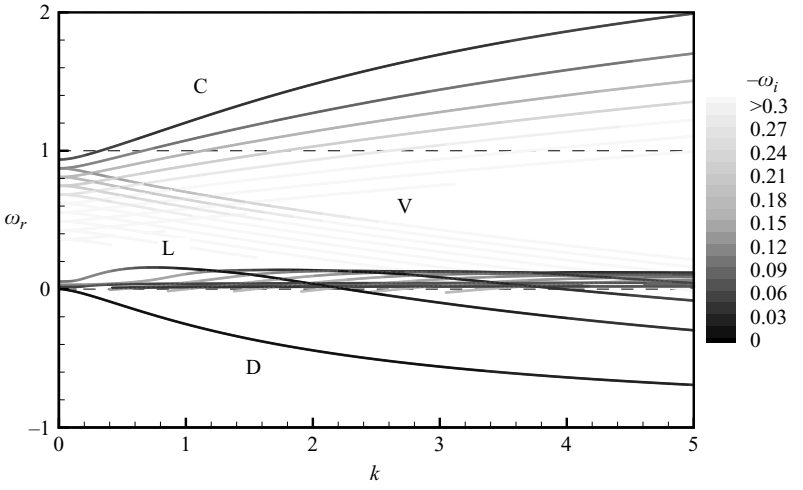

FIGURE 5. Frequencies of the helical ($m = 1$) eigenmodes, for $Re = 1000$.

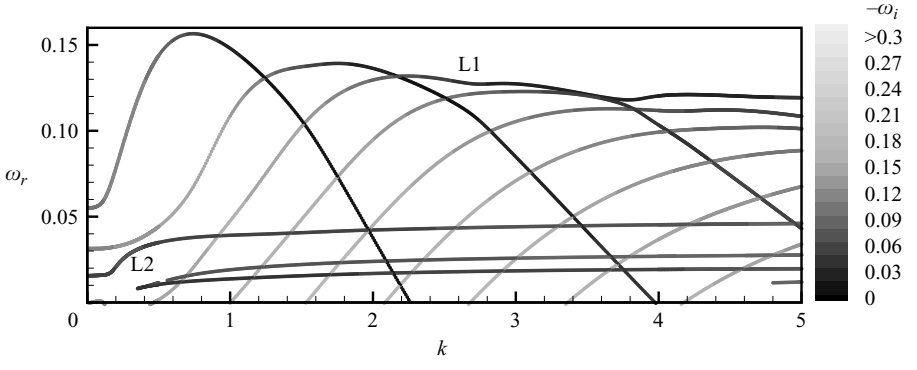

FIGURE 6. As in figure 5, but with a closer view of the frequencies of the L eigenmodes.

third family, called V, are always retrograde, and become strongly damped as their wavenumber is increased. Finally, the branches of the fourth family, called L, are located in the region $-1 < \omega_r < 0.16$. Figure 6 shows a close-up view of these branches, and shows that this family may be further decomposed into two subsets. The first kind of branch, denoted L1, is retrograde for small wavenumbers, but become stationary, and then countergrade, above a particular value of k. The second kind of branch, denoted L2, is always retrograde and displays a different behaviour. At least nine L1 branches and three L2 branches could be computed and are displayed in the figure. In the range of wavenumber displayed two of the L1 branches become countergrade waves, respectively for $k > 2.262$ and $k > 3.975$.

Figure 7 is another illustration of the proposed eigenmode classification. This figure displays, in the complex ω-plane, the discrete eigenvalues (with diamond symbols) computed for a single value of the wavenumber, namely $k = 3$. The four families of waves are clearly separated in this picture. The L1 and L2 subsets of the family L are also identified (for $k = 3$ only one mode of the L1 family is located in the countergrade range).

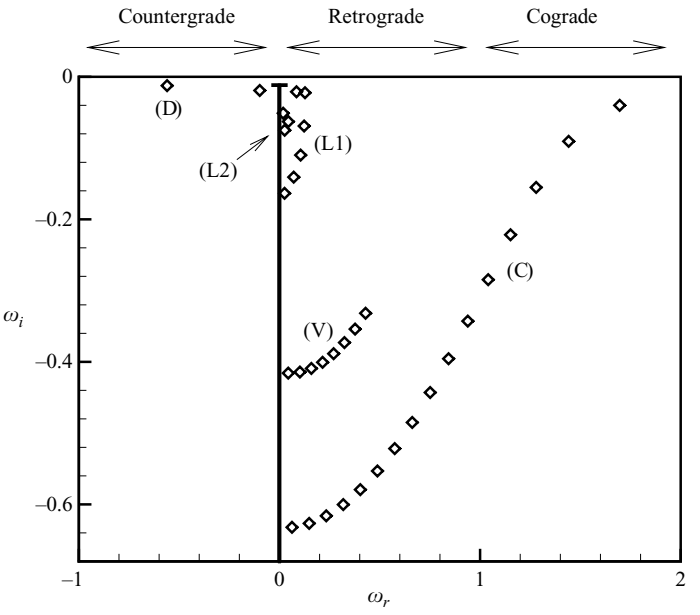

FIGURE 7. Spectrum in the complex ω-plane for $m = 1$, $k = 3$, $Re = 1000$. The diamond symbols and the thick line indicate, respectively, the discrete eigenvalues (computed) and the position of the continuous spectrum (assumed, see Appendix A).

Note that the discrete eigenmodes, considered alone, do not form a complete basis on which to decompose an arbitrary perturbation: a viscous continuous spectrum must also be included, as a consequence of the unbounded nature of the problem. The description of this continuous spectrum is still an open issue. In Appendix A, we present an argument indicating that it is located along the imaginary axis and below the value $\omega = -\mathrm{i}k^2/Re$. This expected continuous spectrum is depicted by a thick line in figure 7.

Compared to the case of a Rankine vortex (e.g. Saffman 1992; Arendt *et al.* 1997), significant differences are observed, and have already been pointed out by Sipp & Jacquin (2003) in the inviscid case. The most striking difference is found in the retrograde range. In this range, the Rankine vortex admits a set of neutral, left-propagating waves, which all start from $\omega = 1$ for $k = 0$ and become countergrade as k is increased, whereas the Lamb–Oseen vortex possesses several families of singular, damped modes. The first family, called L1 here, has already been described by Sipp & Jacquin (2003) in the inviscid case. The other families observed in this interval, called V and L2, are newly discovered.

In the following subsections these four families of modes are successively described. In each case, the physical mechanism responsible for their propagation or attenuation is explained, and the effect of viscosity is detailed.

5.1. *The displacement wave (branch D)*

5.1.1. *Description for* $Re = 1000$

Let us consider, first, the particular branch noted D in the previous figures. This wave has been particularly studied by Leibovich *et al.* (1986), who called it the slow wave because its phase velocity tends to zero as $k \to 0$. Their results show that the properties of this wave weakly depend upon the vortex core details and are generic to all vortex models. In particular, it is the only helical wave to have a full equivalent in the case of a Rankine vortex.

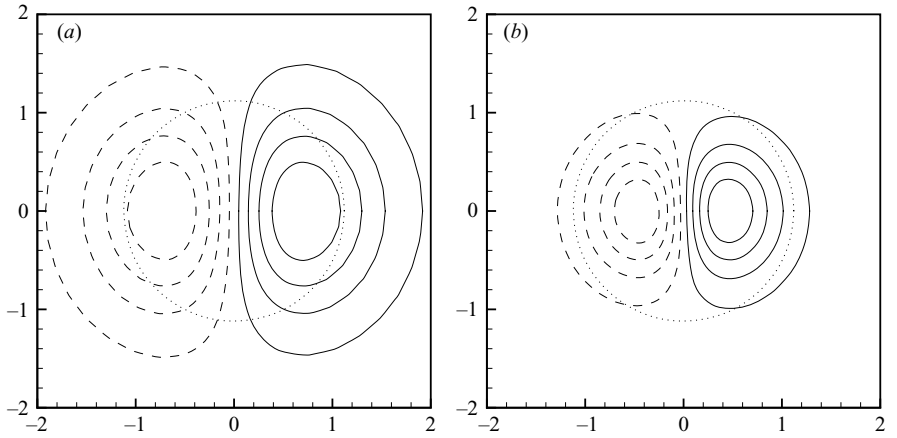

FIGURE 8. Structure of the 'helical displacement wave' for $Re = 1000$; (*a*) $k = 0.1$, $\omega = -0.012 - 4.7 \times 10^{-5}$i; (*b*) $k = 3$, $\omega = -0.5602 - 0.0124$i. Iso-levels of the axial vorticity (ξ_z) component in the (x, y)-plane. Eight equally spaced levels are displayed, and dashed levels correspond to negative values. The dotted circle corresponds to the location of maximum azimuthal velocity at $r = 1.1209a$.

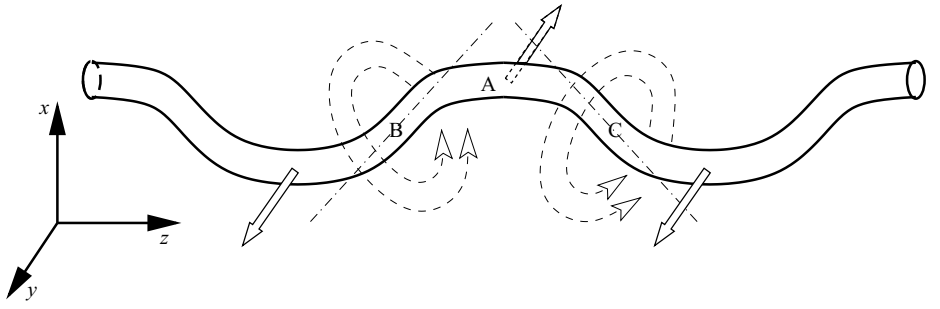

FIGURE 9. The physical mechanism for the helical displacement wave (branch D). See explanations in text.

The structure of this wave is illustrated in figure 8, for $k = 0.1$ and $k = 3$, respectively. The plots display iso-levels of the axial vorticity eigencomponent $\mathrm{Re}[\xi_z(r)\exp(\mathrm{i}m\theta)]$ in a transverse (x, y)-plane. As can be observed, the eigenmode takes the form of a dipole of vorticity and is weakly dependent upon the axial wavenumber. When superimposed onto the base flow, the effect of this dipole is to increase the vorticity in one half of the vortex core, and to decrease it in the other half. Therefore, the net effect corresponds to a displacement of the whole vortex core in a helical way. This justifies the denoting of this wave as a *displacement wave*.

5.1.2. *Physical mechanism*

In the two-dimensional case ($k = 0$), the displacement wave reduces to a simple translation of the vortex and is stationary and neutral ($\omega = 0$). This property simply results from the conservation of momentum (Bernoff & Lingevich 1994). For $k \neq 0$ three-dimensionality leads to a rotation of the wave in a direction opposite to that of the vortex. The physical mechanism responsible for this counter-rotation is explained in figure 9. The figure represents a plane wave which takes the form of a sinusoidally displaced vortex filament located in the (x, z)-plane (such a plane wave can be

constructed as the superposition of two helical waves with $m = \pm 1$, and the physical mechanism is the same for plane and helical waves). On each section of the vortex filament, the velocity can be computed as a Biot-Savart integral expressing the sum of the elementary velocity fields induced by all the other parts of the filament. For long wavelengths it can be expected that the dominant part of the integral will come from the neighbouring parts of the filament. (This approximation is known as the local induction approximation (LIA), and some points of justification are given in Saffman (1992).) Let us apply this argument to evaluate the velocity at a section, labelled A in figure 9, where the x-displacement of the vortex is maximum. The elementary velocity field induced by a section B situated just left of section A takes the form of circular streamlines which encircle the tangent to the axis of the filament in section B. Due to the curvature of the vortex, the point A is located below this tangent line, so the velocity induced in section A is directed towards negative y. Similarly, the elementary velocity field induced at section A by a section C located just right of it is also directed in the negative y direction. This argument may be repeated for other sections of the filament. For example, the velocity induced at sections D and E of the vortex, where the x-displacement is negative, is directed towards positive y. As a consequence, the whole filament tends to precess about the z-axis in a direction opposite to that of the circulation of the vortex.

5.1.3. *Effect of viscosity*

For the case $Re = 1000$ displayed in figure 5, the displacement wave is the least affected by viscosity of all helical waves, and indeed of all Kelvin waves. In the interval $0 < k < 5$, the damping rate always satisfies $|\omega_i| < 0.03$.

As for the axisymmetric waves, the frequency of the helical displacement wave admits a regular development with the form (3.1). In the inviscid case, the behaviour of the frequency as $k \to 0$ was investigated by Leibovich *et al.* (1986), and found to be $\omega^{(0)} = -k^2(\ln(1/|k|) + 0.0577) + O(k^4 \log|k|)$. Inspection shows that in this limit the regular development (3.1) still holds, and that the term $\omega^{(1)}$ is also $O(k^2 \log|k|)$. However, the corresponding coefficient has not been calculated.

5.2. *The core waves (family C)*

5.2.1. *Description for* $Re = 1000$

Let us consider, now, the second family of helical modes, denoted C in figures 5 and 7. Figure 10 illustrates the structure of two eigenmodes computed on the first and second branches of this family, for $k = 5$ and $Re = 1000$. As can be seen, the structure of these modes is located entirely within the vortex core, whose approximate extent is represented by the dotted circles in the plots. The mode on the first branch takes the form of a simple dipole (figure 10*a*). The mode on the second branch is described as two overlapping dipoles (figure 10*b*). Similarly, the modes on the higher branches are multiply overlapping dipoles. The slight reflectional dissymmetry observed in the structure of the modes is, again, an effect of viscosity.

The location of the eigenmodes within the vortex core is one of the distinctive properties of the C family, and justifies the denomination of these waves as *core waves*. An other distinctive property is that, except in the long-wave regime which will be considered below, these waves are essentially cograde.

5.2.2. *Physical mechanism*

The physical mechanism explaining the properties of core waves is illustrated in figure 11. Figure 11(*a*) sketches the structure of a core wave in a plane perpendicular

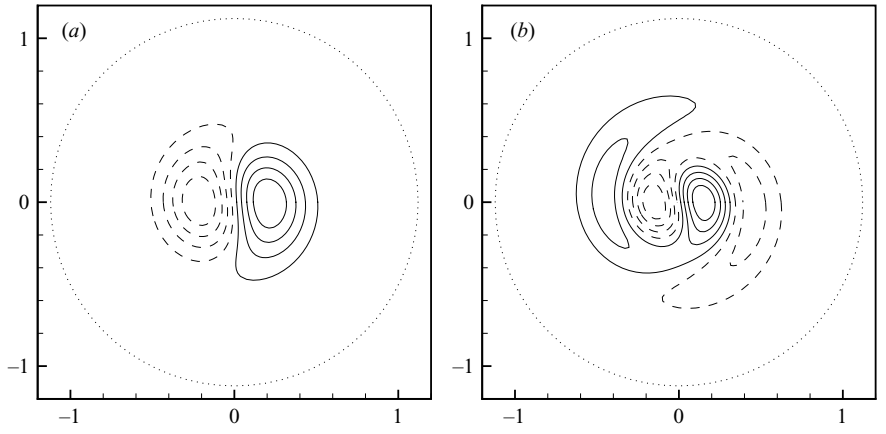

FIGURE 10. Examples of C waves for $m = 1$, $k = 5$, $Re = 1000$; (a) $\omega = 1.9920 - 0.0625\mathrm{i}$; ($b$) $\omega = 1.7031 - 0.1114\mathrm{i}$. Same conventions as in figure 8.

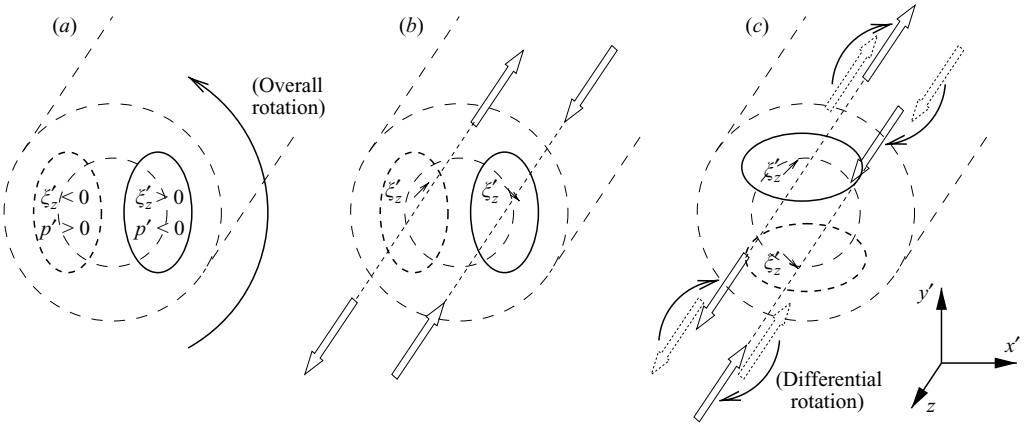

FIGURE 11. The physical mechanism for the C waves. See explanations in text.

to the vortex axis. One recognizes a dipole of axial vorticity ξ_z superimposed onto the vortex and located around its centre. (To picture the three-dimensional structure of this wave, it must be imagined that this dipole is wrapped in a helical way around the vortex centreline.)

Let us follow the evolution of this initial dipole in a reference frame (x', y', z) rotating with the angular velocity of the vortex centreline. At first, as the dipole is entirely located within the vortex core where the rotation rate is almost constant, it experiences at leading order the effect of a uniform background rotation. As a consequence, the left half of the dipole is of anticyclonic nature, and is associated with a high-pressure region. On the other hand, the right half of the dipole of figure 11(a) is of cyclonic nature, and is associated with a low-pressure region.

Now, the effect of these high- and low-pressure regions is to induce an axial flow within the vortex core (depicted by the arrows in figure 11(b)). This axial flow affects, in turn, the vorticity of the base flow. As illustrated in the plot, the axial velocity stretches the left half of the dipole, and compresses its right half. The effect of this stretching/compressing is to increase the vorticity levels in the left half and to decrease the vorticity levels in the right half. Therefore, the initial vorticity dipole tends to reverse its initial orientation.

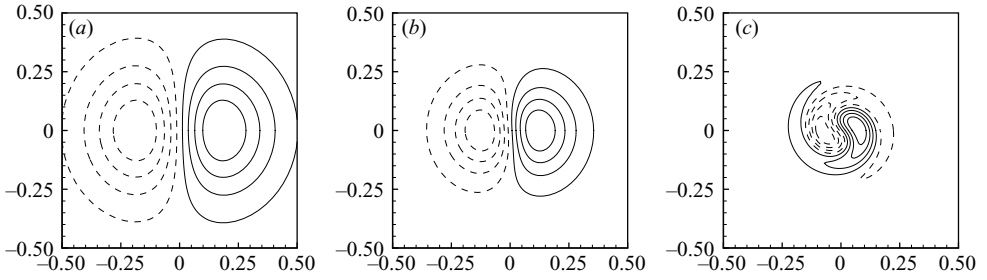

FIGURE 12. Structure of the eigenmode on the first C branch, for $m = 1$, $Re = 10^5$, and various values of the wavenumber k. (a) $k = 1$, $\omega = 1.2099 - 4.01 \times 10^{-4}$i; ($b$) $k = 0.5$, $\omega = 1.0708 - 8.05 \times 10^{-4}$i; ($c$) $k = 0.1$, $\omega = 1.0003 - 5.212 \times 10^{-3}$i. Illustration of the centre-mode behaviour as the wavenumber k is decreased. Same conventions as in figure 8.

This effect, alone, would lead to a wave which is stationnary in the rotating frame, and therefore rotating at exactly the angular velocity of the vortex centreline in the fixed frame. So, there must be an additional effect responsible for the cograde movement. This effect arises from the fact that the rotation of the vortex core is not exactly a solid body rotation, but a differential rotation. When observed from the rotating frame, this differential rotation is observed as a retrograde movement of the parts of the vortex surrounding the axis. As illustrated in figure 11(c), this retrograde flow convects the axial flow. As a result, the part of the vortex which experiences a stretching is not the left half of the dipole, but a region located above. Similarly, the part of the vortex which experiences compression is not the right half, but a region located below. As a consequence, the result of the axial flow is to induce a new dipole which is tilted with respect to the initial dipole in the direction of the vortex rotation. The cograde rotation of the wave is thus explained.

This scenario is of course questionable because it retains only a few of the possible physical mechanisms. However, the retained mechanisms are precisely those which occur at leading order in a long-wave asymptotic analysis (Fabre 2002; Fabre & Le Dizès 2006).

5.2.3. *Effect of viscosity*

The effects of viscosity on the modes described here are shown when comparing the viscous results presented in figure 5 with the inviscid results of Sipp & Jacquin (2003). At first, as could be expected, viscosity leads to a damping of these waves. For $Re = 1000$, the least-damped C wave is found on the first branch for $k = 1.62$ and corresponds to $\omega = 1.3821 - 0.0331$i. A second and less expected effect of viscosity is found in the long-wave range. As can be observed, when the wavenumber is decreased towards zero, all the branches of the C family progressively change from cograde to retrograde. Moreover, the damping rate of the modes, which passes through a minimum for a finite value of k, increases as $k \to 0$. As we shall now argue, these trends are explained by the fact that in this limit, the modes cease to behave as regular Kelvin waves, and become a kind of singular mode called centre modes.

This centre-mode behaviour is best illustrated at a larger value of the Reynolds number. Figure 12 shows the evolution of the eigenmode computed on the first branch of a C wave, for $Re = 10^5$, as the wavenumber k is decreased. Figure 12(a), for $k = 1$, shows the typical dipole structure already described. Figure 12(b) corresponds to $k = 0.5$. As can be observed, the structure of the mode remains essentially the same, but at a smaller scale. This narrowing of the mode structure can be understood in the framework of the physical scenario described above. As the axial gradients

decrease because of the increasing of the wavelength, larger pressure levels in the cyclonic and anticyclonic regions are required to induce the axial flow necessary to sustain the wave. A narrow cyclone (resp. anticyclone) leading to a strong depression (resp. high-pressure region), is realized with a stronger concentration of the vorticity dipole. Note that when k is decreased from 1 to 0.5, the damping rate of the waves is increased by nearly a factor 2. This feature is also fairly well understood, a reminder that stronger radial gradients result in a higher dissipation. In this regime, the waves remain inviscid at leading order and can be identified as *inviscid centre-modes*.

Figure 12(c) corresponds to $k = 0.1$. Now, the structure of the eigenmode has changed dramatically, and has acquired a characteristic spiral shape. By the same time, the damping rate of the mode has strongly increased, and it is now more than ten times higher than the value it had for $k = 1$. In the framework of our physical scenario, these dramatic changes can be understood by supposing that the structure of the mode has become so narrow that the effect of viscosity is now comparable in magnitude with the mechanisms responsible for the wave propagation. In this regime, the structure of the modes becomes viscous at leading order, and they can be identified as *viscous centre-modes*.

All the trends just described are captured well by an asymptotic analysis conducted by Fabre & Le Dizès (2006). In particular, this study shows that the transition from inviscid centre-modes to viscous centre-modes occurs as soon as $k = O(Re^{-1/4})$, and that the frequency then follows a scaling with the form $\omega = m + O(Re^{-1/2})$. On the other hand, it can be checked that for fixed k and $Re \to \infty$, the frequencies of the core waves admit a regular expansion with the form (3.1).

5.3. *The purely viscous modes (family V)*

The third family of modes denoted V in figures 5 and 7, are purely viscous modes, and have no counterparts in the inviscid results of Sipp & Jacquin (2003). One could be tempted to identify them with the inviscid, regular modes which exist in the same range of frequencies for the Rankine vortex. However, inspection shows that the structure of the eigenmodes is completely different.

Two specimens of eigenmodes, computed on the first (i.e. least damped) branch of the family, are displayed in figure 13. For $k = 0.1$ (figure 13a), the eigenmode is very similar to the C mode displayed in figure 12(c), and is characterized by a spiral structure located in the vicinity of the centreline. As can be observed in figure 13(b) corresponding to $k = 1$, increasing the wavenumber results in an extension of the spiral structure, which tends to occupy the whole vortex core, a larger number of spiral turns, and an increase of the damping rate.

In the large-Reynolds-number limit, these modes become centre-modes with a structure very similar to the unstable modes existing in trailing vortices and studied by Fabre & Jacquin (2004b). Le Dizès & Fabre (2006) recently conducted an asymptotic study which encompasses all kinds of viscous centre-modes in the same framework. The present modes correspond to viscous centre-modes of kind C in the nomenclature of Le Dizès & Fabre (2006). The asymptotic prediction for their frequency (valid for $m > 0$) is as follows:

$$w \approx m + 3\mathrm{e}^{-5\mathrm{i}\pi/6}\, k^{2/3} Re^{-1/3} + \left(N + \frac{1}{2}\right)\sqrt{6m}\,\mathrm{e}^{-3\mathrm{i}\pi/4}\, Re^{-1/2} \quad (\text{with } N = 0, 1, 2, \ldots).$$

Numerical results for the Lamb–Oseen vortex are in good accordance with this expression for $Re \geqslant 10^6$, but a detailed comparison is not presented here.

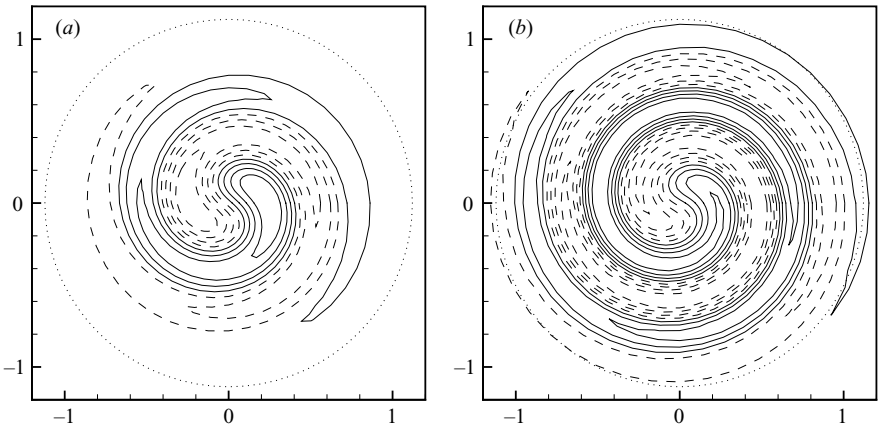

FIGURE 13. Examples of V eigenmodes ($m=1$, $Re=1000$). (a) $k=0.1$, $\omega=0.8664-0.1223\mathrm{i}$; ($b$) $k=1$, $\omega=0.7023-0.1881\mathrm{i}$. Same conventions as in figure 8.

5.4. *The L branches*

Let us consider, now, the last family of helical waves, denoted L in figures 5 and 7, and which are best seen in the close-up view of figure 6. The complete cartography of these waves was particularly tedious and challenging. It required, as a numerical 'trick', the extensive use of a complex mapping function, which is presented in Appendix B.

5.4.1. *Description for* $Re=1000$

Figure 14 represents the structure of the eigenmode belonging to the first L1 branch, for several value of the wavenumber k. Figure 14(a) corresponds to the particular value $k=2.262$, for which the mode is a stationary wave. As can be seen, this wave consists of two overlapping vorticity dipoles. However, contrary to the C mode displayed in figure 10(b), the outer dipole is located on the external parts of the vortex, not entirely within the core.

The stationary nature of this particular wave can be understood as resulting from a competition between the inner and outer dipoles. The outer dipole results in a mean displacement of the vortex centreline which would, alone, lead to a countergrade wave through the mechanism described in § 5.1.2. On the other hand, The inner dipole would, alone, lead to a cograde wave through the mechanism described in § 5.2.2. An equilibrium between these two effects is reached for the particular wavenumber $k=2.262$. For larger wavenumbers, the wave becomes countergrade due to a larger influence of the outer dipole, while for smaller wavenumbers, the wave becomes retrograde due to a larger influence of the inner one.

The evolution of the structure of the eigenmode as the wavenumber is decreased from 2.262 to 0 is very interesting, and is detailed in the next plots. At first, in the range $1.2 \lesssim k < 2.262$, the mode becomes retrograde, but its structure remains that of a regular Kelvin wave, similar to that displayed in figure 14(a). Then, for lower values of the wavenumber, dramatic modifications of the eigenmode structure are observed and are illustrated in figure 14(b–d).

For $k=1$ (figure 14b) one observes the appearance of two spiral arms located in an annular region located outside the vortex core, around $r \approx 2.5$. As the wavenumber is further decreased, this spiral structure progressively acquires a greater importance. For $k=0.8$ (figure 14c), the spiral arms are observed to wind more than one turn, and the vorticity level within the arms is comparable to those in the inner dipole. This kind of perturbation, characterized by the simultaneous presence of a wave-like

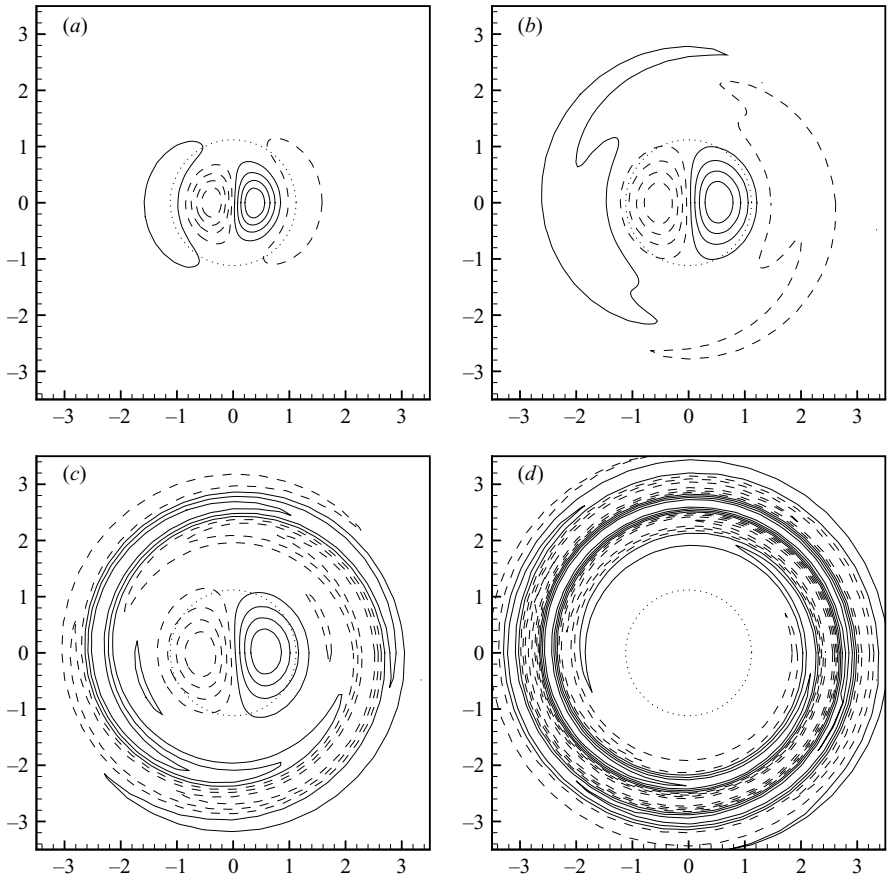

FIGURE 14. Structure of the eigenmode on the first L1 branch, for $m=1$, $Re=1000$, and various values of k. (a) $k=2.262$, $\omega, =-0.0119$i; (b) $k=1$, $\omega=0.1480, -0.0216$i; (c) $k=0.8$, $\omega=0.1560-0.0433$i; (d) $k=0.5$, $\omega=0.1439-0.0900$i. Same conventions as in figure 8.

component and a spiral component, is called a *critical layer wave*, and will be particularly considered in the next subsections.

When the wavenumber is decreased further, the spiral component acquires a greater importance, and eventually dominates the wave component. For example, for $k=0.5$ (figure 14d), nearly three spiral turns are observed, and the wave component cannot be distinguished. In that case, the mode should no longer be called a Kelvin wave, and becomes a truely singular mode. Note that the value $k=0.8$ corresponds approximatily to the case where the oscillation rate ω_r is maximum. Therefore, the observed change of eigenmode structure is associated with a change of behaviour of the branch: from left-propagating (with negative $\partial\omega_r/\partial k$) for $k > 0.8$, the branch becomes right-propagating (with positive $\partial\omega_r/\partial k$) for $k < 0.8$.

Figure 15 displays two other examples of the L family. Figure 15(a) corresponds to an eigenmode belonging to the second L1 branch, for the value of the wavenumber $k=3.975$ where this wave is stationary. As can be observed, the structure consists of three overlapping dipoles. As for the first branch, when the wavenumber is decreased, the structure first remains essentially unchanged (down to $k \approx 2.6$). Then, the mode becomes of the critical layer wave type, with the coexistence of a wave component and a spiral structure (down to $k \approx 1.4$), and finally for even smaller wavenumbers the mode becomes a true singular mode while its direction of propagation is reversed.

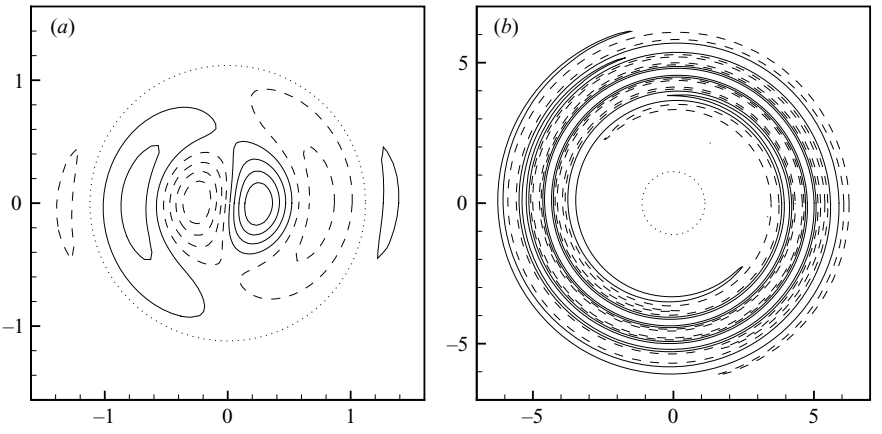

FIGURE 15. Structure of two L eigenmodes: (*a*) $k = 3.975$, $\omega = -0.0368\mathrm{i}$, a mode belonging to the second 'L1' branch, (*b*) $k = 5$, $\omega = 0.04602 - 0.07861\mathrm{i}$, a mode belonging to the 'L2' family. Same conventions as in figure 8, except that in (*b*) only four iso-levels are dislayed.

The eigenmodes computed on the higher branches of L1 waves follow the same trends.

Finally, the mode displayed in figure 15(*b*) belongs to the family of branches identified as L2 in figure 6. This kind of mode looks like the singular modes found on the L1 branches for long wavelengths, as displayed in figure 14(*d*). However, the spiral structure is much more developed, and is located farther from the vortex core. Contrary to the L1 ones, the modes of the L2 branches remain truly singular for all wavenumbers.

5.4.2. *The critical layer waves: physical significance*

The spiral structure described above is the signature of a *viscous critical layer*. The critical layer phenomenon occurs in the vicinity of *critical points* r_c (which may eventually be complex) where the wave is resonant with the mean flow, i.e. where the velocity of the mean flow equals the phase velocity of the wave:

$$m\Omega(r_c) = \omega. \tag{5.1}$$

Because of this resonance, an exchange of energy between the mean flow and the wave is possible, and generally leads to a damping of the wave.

In the vortex literature, the critical layer problem has mainly been investigated in the inviscid, two-dimensional case (Briggs, Daugherty & Levy 1970; Schecter *et al.* 2000), and we begin with a brief review of these studies. In this case, critical layers lead to the existence of damped wave-like perturbations called 'quasi-modes'. Such a perturbation initially behaves as a weakly damped wave located within the vortex. However, at late time, it progressively develops a 'skirt' located in the periphery of the vortex core, where vorticity is continuously wound into a tight spiral, which 'pumps' the energy of the wave and causes its damping. Mathematically, the skirt corresponds to the contribution from the inviscid continuous spectrum (distinct from the viscous continuous spectrum considered in Appendix A). The frequencies of the quasi-modes correspond to the so-called 'Landau poles' whose computation requires a complex contour deformation procedure (see Appendix C where such a calculation is performed). Briggs *et al.* (1970) showed that a condition for waves possessing a critical level to be damped is for the real part of the gradient of the base-flow vorticity at the critical level to be negative, i.e.

$$\mathrm{Re}\left[\Xi'(r_c)\right] < 0. \tag{5.2}$$

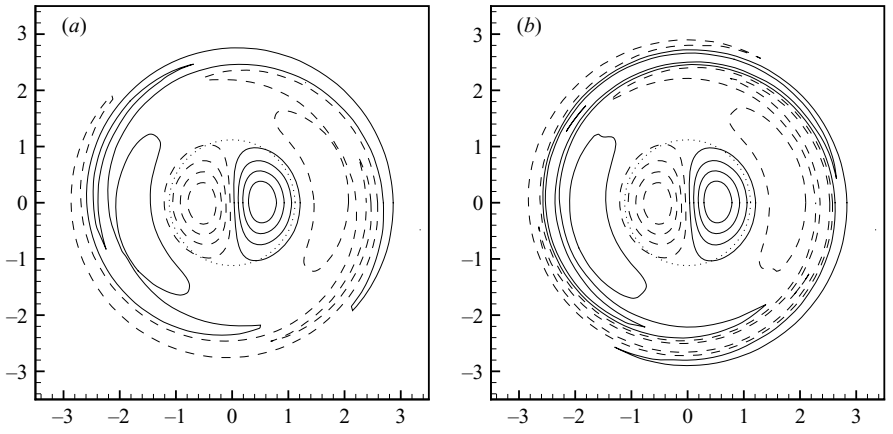

FIGURE 16. The effect of Reynolds number variation on the structure of a 'L' wave (for $m = 1$ and $k = 1$). (*a*) $Re = 3000$, $\omega = 0.1515 - 0.0219\mathrm{i}$; (*b*) $Re = 5000$, $\omega = 0.1522 - 0.0220\mathrm{i}$. Same conventions as in figure 8.

Note that this condition was initially established under more severe hypotheses than in the case we are considering here (the base flow must be close to the Rankine model and the perturbation two-dimensional).

Schecter *et al.* (2000) gave a physical explanation of the condition (5.2), based on the conservation of total angular momentum (see Appendix A of their paper). First, they decompose the angular momentum into a (constant) contribution from the base flow, a contribution from the 'wave', proportional to the square of its amplitude, and a contribution from the skirt. Then, they are able to show that phase mixing of vorticity leads to an increase of the angular momentum contained within the 'skirt', as soon as the condition (5.2) holds. So, the only way for the system to conserve total angular momentum is for the 'wave' amplitude to decay.

Despite their different mathematical nature, the viscous critical layer modes and the inviscid quasi-modes describe the same physical reality: the coupling between the intrinsic dynamics of a vortex core and the winding of perturbations located in its periphery. The difference between the two kinds of perturbations is that in the inviscid case, the winding never reaches an asymptotic state, and the narrowing of the spiral arms occurs indefinitely. On the other hand, in the presence of viscosity, the narrowing of the spiral arms leads to an increase of the radial gradients which enhance the dissipation. Thus, the winding does not occur endlessly, but up to a time when dissipation becomes non-negligible. According to this explanation, the 'skirt' of spiral arms of the quasi-modes and the spiral region of the critical layer waves play the same role. The difference is that in the first case, the energy lost by the wave is transferred into the skirt region where it results in an increase of the mean angular momentum, whereas in the second case, it is dissipated through the effect of viscosity.

Following this explanation, for a given mode, the higher the Reynolds number, the narrower the spiral arms have to be to provide the right amount of dissipation. This prediction is checked in figure 16, which shows the effect of Reynolds number variation on the eigenmode already displayed in figure 14(*b*). As can be seen when comparing these plots, when the Reynolds number is raised from 1000 to 5000, the only noticeable change in the eigenmode structure is the predicted narrowing of the spiral arms.

Note, finally, that for the Lamb–Oseen vortex, all retrograde modes possess a critical point satisfying the condition (5.2), and should therefore be damped through

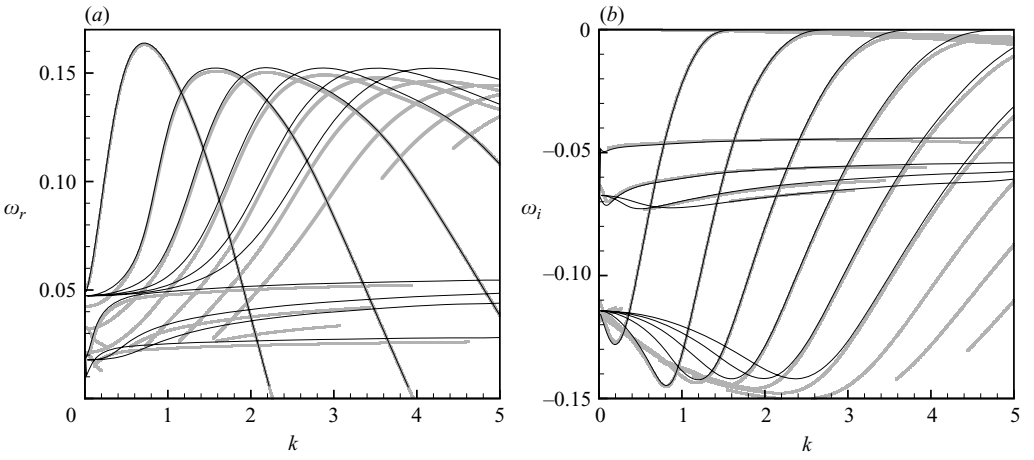

FIGURE 17. Oscillation rates (*a*) and damping rates (*b*) of modes computed in the viscous and inviscid cases. Thick grey lines: viscous results for $Re = 10^4$. Thin black lines: inviscid results obtained using the complex contour deformation procedure (selected branches from figure 27).

the mechanism described above. However, as noted in the previous section, critical layer waves, characterized by the coexistence of a wave component and a spiral structure, are only observed on each L1 branch in a narrow range of wavenumbers, which is bounded from above by the point where the oscillation frequency is about $\omega_r \approx 0.12$ (i.e. $k \approx 1.2$ for the first L1 branch, $k \approx 2.6$ for the second branch, etc.), and from below by the point where the direction of propagation of the mode reverses (i.e. $k \approx 0.8$ for the first L1 branch, $k \approx 1.4$ for the second branch, etc.). Above this range, the modes are regular waves, and below the modes only possess the spiral component. Incidentally, in their inviscid asymptotic study, Le Dizès & Lacaze (2005) report the occurrence of a bifurcation in the mathematical structure of the modes for $\omega = 0.1267$. However, a physical argument explaining why this transition occurs for this precise value is missing.

5.4.3. *The large Reynolds number limit*

It is important to understand that, although dissipation is eventually achieved through the effect of viscosity within the spiral region, the mechanism responsible for the damping of the critical layer waves is essentially inviscid. Accordingly, the frequencies (and damping rates) of these waves are expected to match, as the Reynolds number tends to infinity, with those of the 'inviscid singular modes' computed using a contour deformation procedure.

A family of such waves has been computed by Sipp & Jacquin (2003), and their asymptotic properties have been explored by le Dizès & Lacaze (2005). This family will be called here 'inviscid singular modes of the first kind'. With extensive use of the contour deformation procedure, we have discovered at least two other families, which are called inviscid singular modes of the second kind and of the third kind. The reader will find in Appendix C a mapping of these new modes (figure 27), and a few arguments justifying their occurrence. The object of this section is simply to compare the frequencies of these inviscid singular modes with those of the L modes computed in the viscous case.

Figure 17 compares the real and imaginary parts of the frequencies of the modes computed in the viscous (with $Re = 10^4$) and inviscid cases. As can be observed, at

Re	ω	$(\omega-\omega^{(0)})\times Re$
10^3	0.14803556–0.02167704i	–5.2096+0.3904i
10^4	0.15272368–0.02200868i	–5.2155+0.5875i
10^5	0.15319309–0.02206135i	–5.2139+0.6083i

TABLE 1. Illustration of the asymptotic behaviour of the frequency with large Reynolds numbers, for a critical layer wave with $m=1$, $k=1$. The inviscid limit, computed using the contour deformation procedure, is $\omega^{(0)}=0.15324523-0.02067435\mathrm{i}$.

least nine viscous branches, belonging to the subset L1, match with inviscid branches of the first kind. Three viscous branches of the subset L2 match with inviscid branches of the second kind, and one with an inviscid branch of the third kind.

The way the inviscid limit is approached remains to be described in detail. The simplest guess is to assume that the frequency ω follows a development in powers of Re^{-1}, with the form given by equation (3.1). If the frequency is to follow such a development, then the quantity $(\omega-\omega^{(0)})\times Re$, where $\omega^{(0)}$ is the inviscid limit, should asymptote to a finite limit as $Re\to\infty$. This prediction is checked in table 1, which displays this quantity computed for the L eigenmode already considered in figures 14(b) and 16. These results confirm the prediction, and give the approximate value of the second term in the development: $\omega^{(1)}\approx -5.21+0.61\mathrm{i}$.

Note, finally, that in figure 27 the viscous results depart from the inviscid ones in the long-wave range. Inspection shows that in this case, the frequencies evolve in powers of $Re^{-1/2}$ instead of Re^{-1}, just as for the C waves. This limit has not been investigated further.

5.4.4. *Structure of the modes in the complex r-plane*

We have observed in the previous section that the frequencies of the critical layer waves evolve in powers of Re^{-1}, with the form given by equation (3.1). However these modes are not regular Kelvin waves in the usual sense, because the corresponding eigenmodes $\boldsymbol{u}(r)$ do not admit a regular development with the form (3.2) – at least for real values of r.

In such cases, a better description may be obtained when considering the eigenmode structure $\boldsymbol{u}(r)$ as a function of the complex variable r, obtained through analytic continuation. In that case, it is known that the regular development for the eigenmode structure is invalid in some viscous sectors where the solution is viscous at leading order (Drazin & Reid 1981). This property was initially demonstrated in the case of plane parallel flows by Lin (1955). A rigorous demonstration that this property also holds for swirling flows was obtained recently by Le Dizès (2004). Most specifically, he showed that the eigenmode structure is strongly oscillating in at least one of the sectors delimitated by the *Stokes lines* originating from the critical points r_c, and defined by

$$\arg(r-r_c)=\pi/2+2n\pi/3-\alpha,\qquad \text{with } \alpha=\arg(-\Omega'(r_c))/3. \tag{5.3}$$

Let us check these predictions for the case of the eigenmode corresponding to $m=1$, $k=1$, already displayed in figures 14(b) and 16. For this case, the leading-order frequency, computed using the inviscid equations and the complex contour deformation procedure, is $\omega=0.1532-0.02207\mathrm{i}$, and the corresponding critical point is $r_c=2.5335+0.1832\mathrm{i}$. The Stokes lines are given by equation (5.3), with $\alpha=-0.06914\equiv -3.96^\circ$.

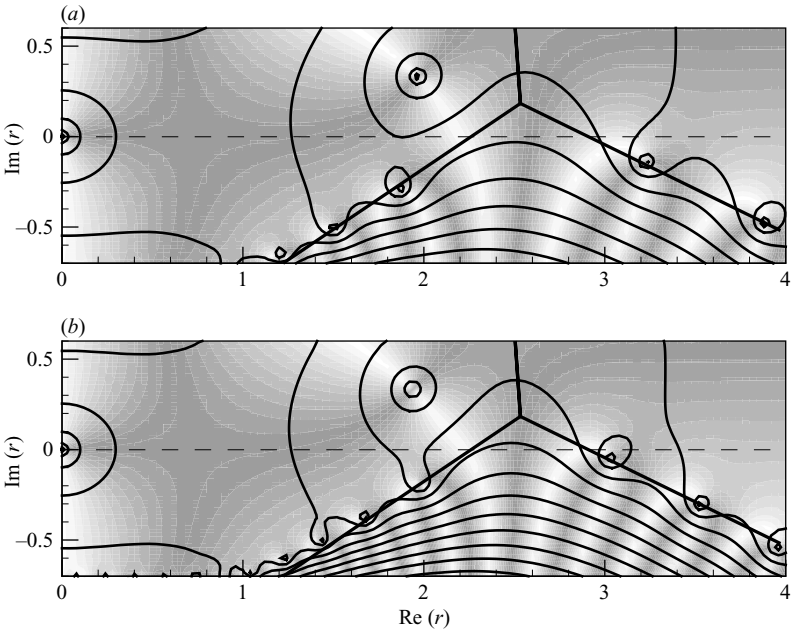

FIGURE 18. Structure of a critical layer wave in the complex r-plane, for $m = 1$ and $k = 1$. (*a*) $Re = 1000$; (*b*) $Re = 2000$. Curves are iso-levels of the modulus (logarithmically spaced), and grey levels indicate the phase, from pure real (dark grey) to pure imaginary (white). The thick straight lines correspond to the theoretical Stokes lines according to Le Dizès (2004).

Figure 18 displays the eigencomponent $p(r)$ in a strip of the complex r-plane surrounding the real axis†. Figure 18(*a*) is for $Re = 1000$, and 18(*b*) is for $Re = 2000$. Curves are iso-levels of the modulus, and grey levels indicate the phase, from pure real (dark grey) to pure imaginary (white). The three thick straight lines are the predicted Stokes lines. As can be observed, in the two upper Stokes sectors, the eigenmode structure is smooth and not affected by variations of the Reynolds number. On the other hand, in the third sector, the solution is highly oscillatory, and the number of oscillations increases with the Reynolds number. It can be observed, finally, that the zeros of the complex function $p(r)$ tend to align along the two lower Stokes lines. This property is generic to the generalized Airy functions with a balanced/dominant behaviour (Drazin & Reid 1981).

The representation given in figure 18 may help in understanding the occurrence of the spiral region from a mathematical point of view: this spiral region is simply the intersection of the viscous sector with the real r-axis. Moreover, this representation gives a formal justification for the contour deformation procedure used in the inviscid case, and for the complex mapping method used in the viscous case. In effect, to

† The procedure used to draw these plots takes advantage of the properties of the Chebyschev collocation method. In effect, when using such a method, the eigenmodes are implicitly known in terms of a polynomial expansion of the mapped variable ξ. This polynomial is readily evaluated for complex values of ξ, which correspond to complex values of r through the mapping function. Note that this procedure differs from that described in Appendix B to design a complex mapping function. Here, the real mapping function defined by equation (B 1) is used, and so the inversion of the eigenvalue problem initially provides the solution for real r. The evaluation of the polynomials for complex arguments is done afterwards.

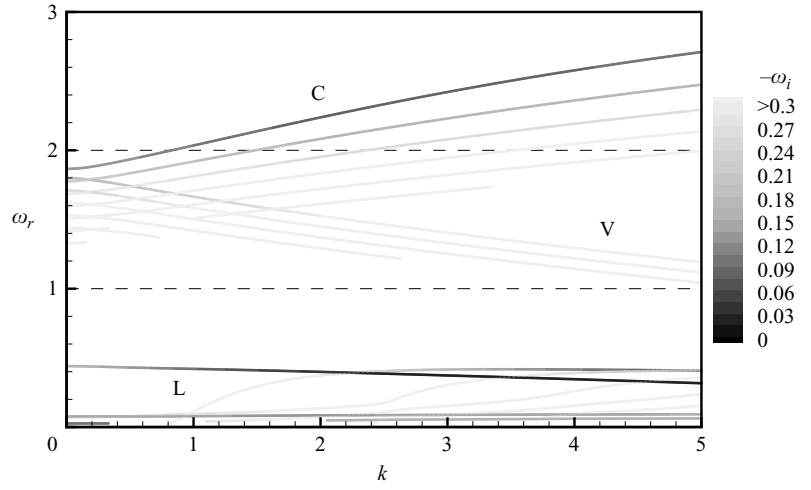

FIGURE 19. Frequencies of the double-helix ($m = 2$), for $Re = 1000$.

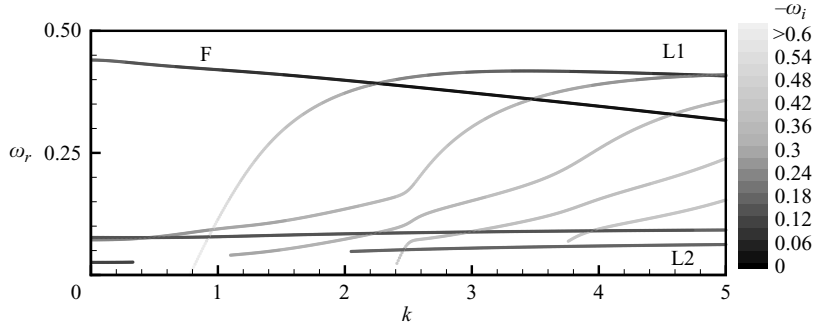

FIGURE 20. As in figure 5, but with a closer view of the L branches.

be precise the idea of these methods is to solve the stability equations along a path which avoids the viscous sectors.

6. Double-helix modes ($m = 2$) and higher azimuthal wavenumbers

Figure 19 displays the frequencies of left-handed double-helix ($m = 2$) modes computed for $Re = 1000$ (with the same conventions as in figures 2 and 5). Three families of branches can be distinguished, and are labelled C, V and L because of their similarities with the corresponding families for $m = 1$. Note that a main difference with the $m = 1$ case is the absence of countergrade modes. In particular, the D branch is absent, and the L waves remain retrograde for all values of k. Figure 20 shows a close-up view of the L family for the range $0 < \omega_r < 0.5$. This family can be further decomposed into two subsets, called L1 and L2. One branch of the L1 family is labelled F and will be particularly considered in the following.

A comparison with the case of a Rankine vortex leads to the same conclusions as for $m = 1$. In particular, the largest differences are found in the retrograde range, where all the modes become more or less damped.

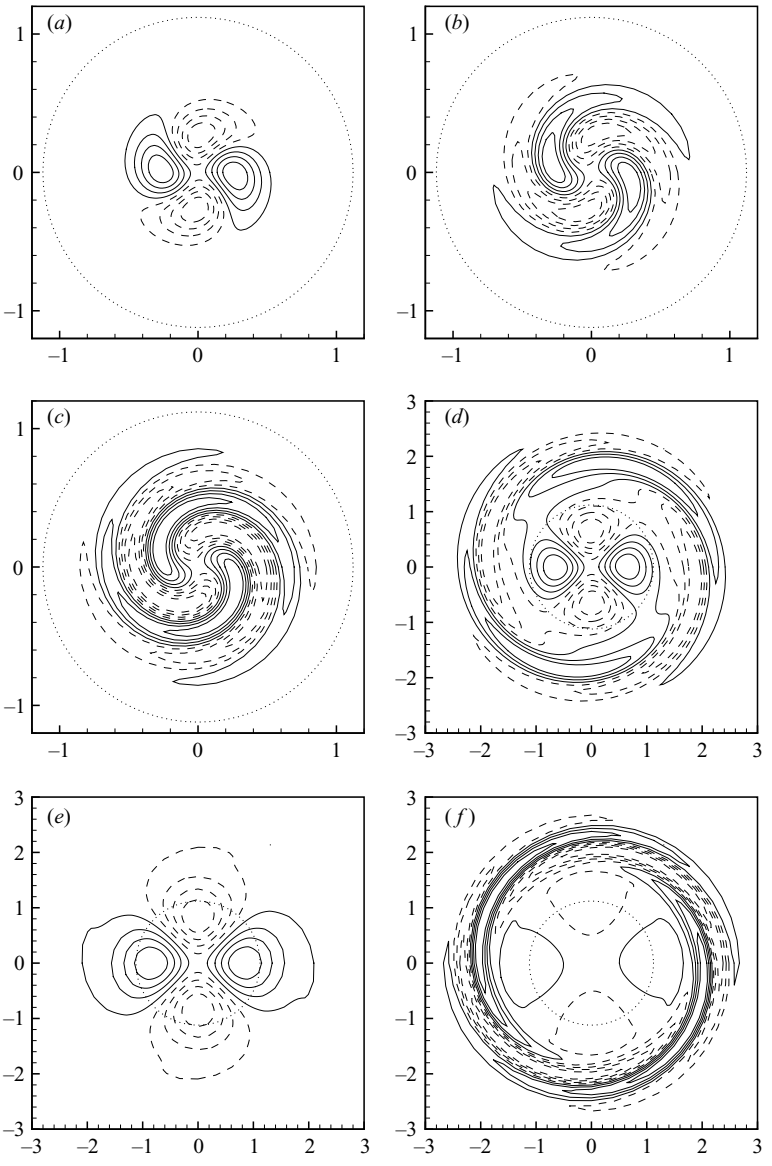

FIGURE 21. Structure of some double-helix eigenmodes ($Re = 1000$). (*a*) C mode with $k = 5$, $\omega = 2.703 - 0.0996\mathrm{i}$; (*b*) C mode with $k = 0.1$, $\omega = 1.8702 - 0.1305\mathrm{i}$; (*c*) V mode with $k = 1$, $\omega = 1.6648 - 0.2339\mathrm{i}$; (*d*) L mode with $k = 5$, $\omega = 0.4077 - 0.0730\mathrm{i}$; (*e*) F mode with $k = 3.45$, $\omega = 0.3608 - 0.0173\mathrm{i}$; (*f*) F mode with $k = 1$, $\omega = 0.4203 - 0.0921\mathrm{i}$. Same conventions as in figure 8.

6.1. *The core waves (family C) for* $m = 2$

The branches of the C family display the same trends as their $m = 1$ counterparts: they are right-propagating and generally cograde ($\omega_r > 2$), except in the long-wave range where they become retrograde ($0 < \omega_r < 2$). An example of an eigenmode belonging to this family is depicted in figure 21(*a*). This eigenmode has some resemblance with its $m = 1$ counterpart displayed in figure 12(*a*). It can be described as a vorticity quadripole located entirely within the vortex core. The waves on the other C branches have a similar structure, with an increasing number of overlapping quadripoles, but

their structure always remain concentrated within the vortex core. Consequently, just as for $m=1$, these waves can be identified as *core waves*. The cograde nature of these waves can be explained with the same physical arguments as those given for $m=1$ in figure 12, except that the geometry is slightly different.

Inspection of the effect of viscosity on these C waves leads to the same conclusions as for $m=1$. On each branch, the damping rate reaches a minimum for a finite value of the wavenumber. For example, for the first (and least damped) branch, the minimum occurs for $k=2.7$, and corresponds to $\omega=2.3690-0.0822\mathrm{i}$. Note that these waves are always substantially more damped than their $m=1$ counterparts (recall that the minimum damping rate for helical C waves is -0.0331). Finally, in the long-wave limit, the present waves also display a centre-mode behaviour. For example, figure 21(*b*) displays the eigenmode computed on the same branch as that in figure 12(*b*), but for $k=0.1$. One can recognize the characteristic centre-mode structure already described in figure 12(*c*) for $m=1$.

6.2. *The viscous modes (family V) for* $m=2$

A second family is recognized as the equivalent of the V modes described for $m=1$. These modes are always countergrade and become strongly damped as the wavenumber is increased. An example of this family is displayed in figure 21(*c*). One sees the typical spiral structure already described for their $m=1$ counterparts (compare with figure 13*b*). The difference is, of course, that the present ones consist of four spiral arms, instead of two arms for $m=1$.

6.3. *The L branches for* $m=2$

The third family is related to the L modes described for $m=1$. The frequencies of these modes are best depicted in the close-up view of figure 20. Note that the grey-scale is different to that used in the previous figures. Accordingly, most of these modes are much more damped than their $m=1$ counterparts. Figure 21(*d*) displays an example of an eigenmode belonging to that family. The structure of this mode is clearly of the critical layer wave type, with the coexistence of a quadripolar wave component within the vortex core, and of a spiral structure located outside of the vortex core. As for $m=1$, the coexistence of both the core wave component and the critical layer only occurs in a limited range of k. The mode corresponding to figure 21(*d*) loses the spiral structure and becomes a regular wave for $k\approx 8$, which corresponds approximately to $\omega\approx 0.39$. On the other hand, it loses the wave component and becomes a true singular mode for $k\approx 3$, which corresponds to the maximum value of ω_r for this mode. The modes on the higher branches seem to display the same trends, and are of the critical layer wave type for ω_r between 0.39 and their maximum value. There is no physical argument explaining these boundaries, but incidentally, as for $m=1$, the value $\omega=0.3871$ corresponds to a bifurcation in the mathematical structure of the modes according to the inviscid asymptotic study of Le Dizès & Lacaze (2005).

The large Reynolds number limit of the L modes for $m=2$ has been investigated in the same way as in § 5.4.3 for $m=1$. Here again, the frequencies are expected to match, at leading order, with those of 'inviscid singular modes' computed using a contour deformation procedure. A mapping of these inviscid singular modes is presented in Appendix C (figure 28). As for $m=1$, in addition to the first kind of waves already computed by Sipp & Jacquin (2003), some new kinds of waves were discovered. Figure 22 compares the real and imaginary parts of the frequencies of the modes computed in the viscous (with $Re=10^4$) and inviscid cases. As can be seen, at least 8 inviscid branches are effectively approached by the viscous results. Note that the inviscid results display a complicated behaviour which was partially explained

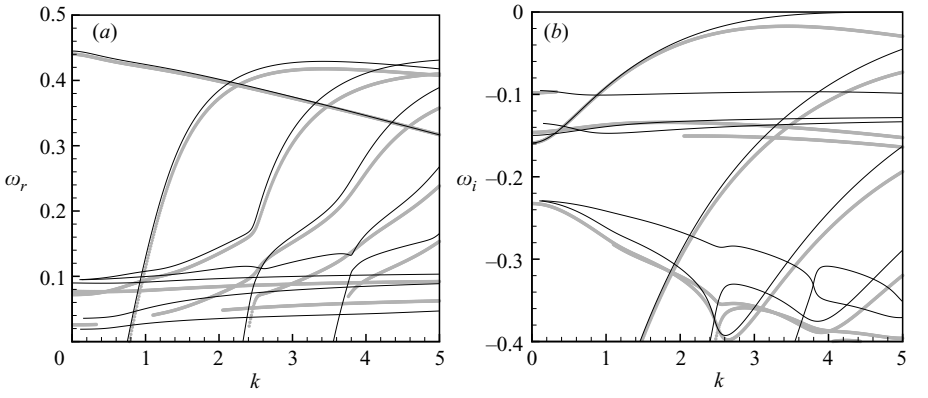

FIGURE 22. Oscillation rates (a) and damping rates (b) of double-helix L waves computed in the viscous and inviscid cases. Thick grey lines: viscous results for $Re = 10^4$. Thin black lines: inviscid results obtained using the complex contour deformation procedure (selected branches from figure 28).

by le Dizès & Lacaze (2005). The viscous results look comparatively more regular, and some kind of mode switching seems to occur (i.e. some viscous branches seem to 'jump' from one inviscid limit to another).

6.4. *The F branch*

6.4.1. *Description*

We have left till the end the description of the particular branch called F in figure 20. For $Re = 1000$, this mode is the least damped of all the $m = 2$ modes. The minimum damping rate occurs for $k = 3.45$, and the corresponding frequency is $\omega = 0.3608 - 0.0173\mathrm{i}$. The corresponding eigenmode is displayed in figure 21(e). This eigenmode takes the form of a quadripole of vorticity which is not confined within the vortex core, but also extends to the outer parts of the vortex. This structure is the simplest of all $m = 2$ modes and has a clear geometrical interpretation. In effect, when superimposed onto the base flow, the effect of this quadripole is to increase the base-flow vorticity along one direction (the horizontal direction in figure 21e), and to decrease it in the perpendicular direction (the vertical direction in figure 21e). Therefore, the net effect of this wave is to deform the vortex core in an elliptical way. This justifies the description of this wave as a *flattening wave*.

For wavenumbers larger than $k = 3.45$, this mode remains a regular weakly damped wave. On the other hand, for lower values of k, the structure changes dramatically. This is illustrated in figure 21(f), for $k = 1$. In that case, one recognizes the now familiar structure of a critical layer wave. For even smaller wavenumbers, the damping rate increases substantially, and for $k = 0$, this mode becomes a highly damped one, with $\omega = 0.4402 - 0.1588\mathrm{i}$.

6.4.2. *Physical mechanism*

The F branch described here has an equivalent in the Rankine vortex, which is called the 'isolated branch' by Eloy & Le Dizès (2001) and Fukumoto (2003), and whose angular velocity ω/m varies between $1/2$ (for $k = 0$) and 0 (for $k \to \infty$).

A physical argument has been proposed by Arendt *et al.* (1997) to explain the properties of this wave. This argument is presented in figure 23. Let us consider a Rankine vortex, with radius a, rotation rate Ω_0, and circulation $\Gamma_0 = 2\pi\Omega_0 a^2$,

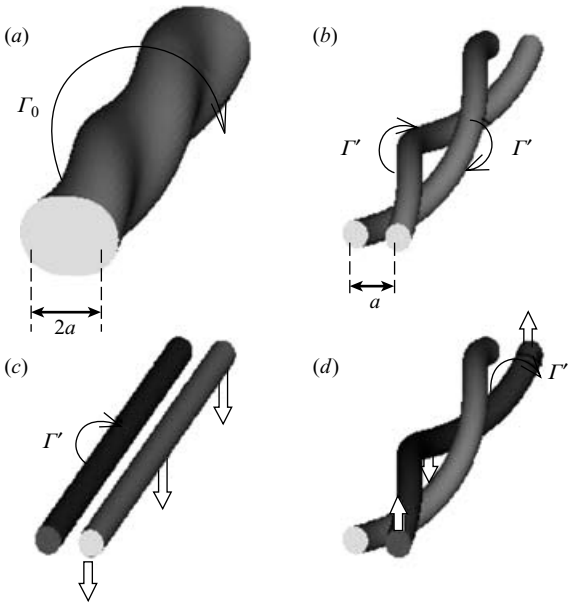

FIGURE 23. The physical mechanism explaining the properties of the F wave, according to Arendt *et al.* (1997). See explanations in text.

deformed by a 'flattening wave' of wavenumber k, as shown in figure 23(a). Arendt *et al.* (1997) argued that this deformed vortex can be modelled as a pair of vortex filaments wrapped around each other in a helical way, located at a distance a from each other, each of them bearing a circulation $\Gamma' = \Gamma_0/2$ (figure 23b).

Let us first consider the two-dimensionnal situation (figure 23c). In this case, each filament is advected by a velocity induced by the other one, of amplitude $\Gamma'/(2\pi a) = \Omega_0 a/2$. For example, the plot shows with arrows the velocity induced by the dark filament on the light one. Therefore, the pair rotates in the positive direction with an angular frequency $\Omega_0/2$, which is precisely the expected angular frequency for the wave.

In the three-dimensionnal case, in addition to the velocity induced by the other one, each filament is advected by its self-induced velocity. This second effect is sketched in figure 23(d). Each filament is displaced in a helical way, and we recognize in this form the presence of a displacement wave. As we know from § 5.1, the velocity induced by these displacement waves would, alone, make the filaments rotate in the negative direction. For example, the plot shows with white arrows the velocity induced by the dark filament on itself. Therefore, the self-induction opposes to the effect of the mutual induction. As a result, in the three-dimensional case, the angular frequency of the wave is lower than $\Omega_0/2$. Moreover, in the short-wave limit, both effect cancel, and the angular frequency tends to zero.

With the results presented in the previous section in mind, we must admit that the scenario presented above, although very seducing and quite accurate for the Rankine vortex, is only partially valid for more realistic vortices such as the Lamb–Oseen vortex. This scenario only remains accurate in the short-wave range, where the F wave effectively reduces to a simple flattening of the vortex. On the other hand, in the long-wave range, the F mode cannot be identified anymore as a flattening wave. For instance, in the two-dimensional limit, the mode is a highly damped one with

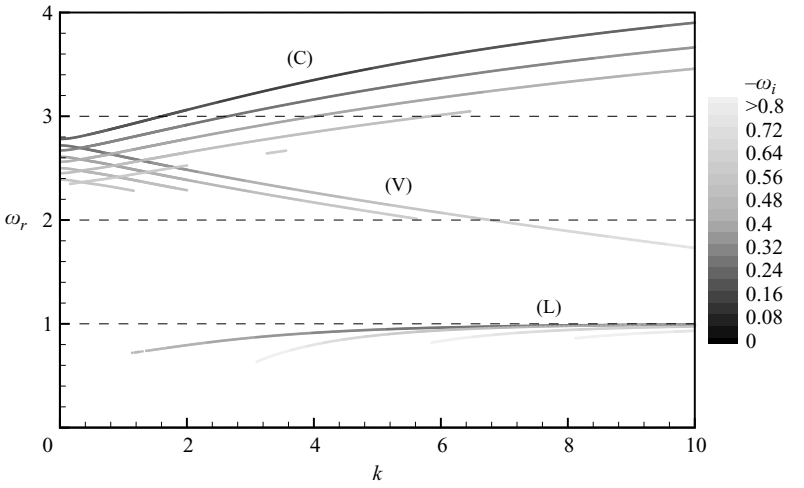

FIGURE 24. Frequencies of the triple-helix ($m = 3$) eigenmodes, for $Re = 1000$.

frequency $\omega = 0.4402 - 0.1588\mathrm{i}$, a value which substantially differs from the value $\omega = 1$ predicted above. In that case, the underlying physical mechanism is completely different, and must include the coupling between the intrinsic dynamics of the vortex core and the winding of perturbations located in its periphery.

Due to these differences, it can be expected that for a Lamb–Oseen vortex the evolution of an initially localized elliptic deformation of weak amplitude will be completely different than in the case of a Rankine vortex considered by Arendt *et al.* (1997). This point is fully confirmed by a study of the initial value problem (Fabre 2002). Note, however, that these conclusions only hold in the linear regime. For perturbations of sufficiently large amplitude, nonlinearities could change the properties of the critical layer and lead to the existence of a 'true' flattening wave for all wavenumbers.

6.5. *Triple-helix modes* ($m = 3$) *and higher azimuthal wavenumbers*

Finally, our survey of the Kelvin waves and viscous modes of the Lamb–Oseen vortex would not be complete if we stopped at the double-helix ($m = 2$) case, and we should also discuss the higher azimuthal wavenumbers. Figure 24 displays the frequencies of the modes with a triple-helix ($m = 3$) geometry. Three families of branches can be found, denoted again C, V and L. In the short-wave limit, the frequencies of all the L modes tend to $\omega_r \approx 1$, a property that was predicted in the large-k inviscid asymptotic analysis of Le Dizès & Lacaze (2005). Note that the greyscale is different to that used in the previous cases. Accordingly, the $m = 3$ modes are much more damped than those with lower m. For $Re = 1000$, the least-damped wave occurs on a C branch for $k = 3.6$, and its frequency is $\omega = 3.2958 - 0.1537\mathrm{i}$. The least damped L wave occurs for $k = 8.78$ and corresponds to $\omega = 0.9887 - 0.2349\mathrm{i}$. The next cases ($m \geqslant 4$) display the same tendencies, with all the modes getting more and more damped. Finally, an equivalent of the F branch described for $m = 2$ does not seem to exist for $m \geqslant 3$.

7. Summary and conclusions

The goal of this study was to describe the normal modes existing on a 'realistic' vortex, the Lamb–Oseen model, and to compare the results with the more academic

case of a Rankine vortex, initially considered by Lord Kelvin (1880), and still used in most studies on vortex dynamics. The complete mapping of all the normal modes turned out to be a numerical challenge, and required, among other numerical tricks, the extensive use of a complex mapping function. Several qualitative differences were found. The most important one is that in addition to regular waves, the Lamb–Oseen vortex also possesses singular viscous modes which are always significantly damped, even in the limit of vanishing viscosity. Another important conclusion is that no amplified modes were found, a result which demonstrates the stability of the Lamb–Oseen vortex. This conclusion may seem obvious. However, the effect of viscosity on swirling flows is highly non-trivial, and viscous instabilities were recently discovered in other kind of vortices which were generally considered as stable (Fabre & Jacquin 2004).

To conclude this paper, we would like to review, once again, the different families of modes, and to comment on their physical relevance to the dynamics of realistic vortices.

The 'Kelvin waves' can be classified into three groups. The first group comprises the axisymmetric waves, the helical displacement wave, and to a lesser extent, the waves found on the L1 and F branches in the range of short wavelengths where they are not affected by the critical layer phenemenon. The waves of this group share a number of similarities. First, they have a direct counterpart in the case of the Rankine vortex. Secondly, they are weakly affected by viscosity, in the sense that they admit a regular development in the limit of large Reynolds number. Third, they have a clear physical mechanism, which can be explained without reference to the precise vortex model. Fourth, and perhaps the most important point, they have all been observed to occur in realistic vortex flows. For example, in their numerical simulation of a turbulent flow resulting from the breaking of an internal gravity wave, Fritts, Arendt & Andreassen (1998) identified characteristic event which can be interpreted as the propagation of axisymmetric, helical and flattening waves. This kind of event seems to play a major role in the energy cascade towards smaller scales in turbulent flows. The physical significance of all these waves is clear: they are responsible for the propagation of disturbances and kinetic energy along a vortex tube.

The second group is formed by the core waves (C branches). These waves fulfil the two first properties listed above: they are qualitatively similar to waves existing in the Rankine vortex and are regular with respect viscosity (although their damping rates are generally higher than for the first group of waves listed above). However, the physical significance of these waves is less clear. In particular, they do not seem to have ever been observed in realistic vortex flows. The reason may be that their structure is located entirely within the vortex core. So, these waves may be present in vortex cores and participate to the propagation of energy, but may be in some way invisible from the outside of the vortex.

The third group is formed by the critical layer waves, which are found on each of the L1 branches in a narrow range of wavenumbers (limited, from above, by the wavenumber corresponding to $\omega_r \approx 0.12$ for $m = 1$, and $\omega_r \approx 0.39$ for $m = 2$, and from below by the wavenumber for which the group velocity changes its sign), and on the F branch for long wavelengths. These waves have no counterparts in the case of the Rankine vortex, and the effect of viscosity on them is highly non-trivial. Due to their particular structure, these waves allow, in some way, a 'communication' between the vortex core and the regions located outside the core. Consequently, they are physically significant in all situations where a transfer of energy occurs between the vortex core and its surroundings. Such a transfer takes place in a 'quasi-mode', a

particular perturbation which initially behaves as a Kelvin wave in the vortex core, but progressively transfers its energy to an annular external region where a resonance occurs. The relevance of critical layer waves to this mechanism has been pointed out. The opposite situation occurs in the interaction of a vortex with an external turbulent field, where an external perturbation can transfer its energy into the inner core. This was recently demonstrated in the optimal perturbation analysis of Antkowiak & Brancher (2004), who observed that the largest transient energy growths occur precisely in the ranges of wavenumbers corresponding to critical layer waves.

Aside from these three groups of Kelvin waves, we have also found that the Lamb–Oseen vortex possesses viscous singular modes of a completely different nature. Mathematically, these modes can be classified into 'inviscid singular modes', when their frequency admits a regular limit as $Re \to \infty$ (L2 modes for all wavelengths, and L1 modes for long wavelengths), and 'viscous singular modes' when they do not behave in this way (V modes, and centre modes in the long-wave limit of the C branches). All these modes are substantially more damped than the waves listed above, and therefore, they are not expected to play any important physical role when considered individually.

Although the tracking of damped modes proved to be an endless task, we can reasonably claim that the cartography presented here is exhaustive. However, there are necessarily open issues, and this work may be followed in several directions.

First, our study was restricted to long and medium wavelengths. The short-wavelength regime was investigated by Le Dizès & Lacaze (2005) using asymptotic methods, but only in the inviscid case. The effect of viscosity in this range is also a matter of interest.

Secondly, we restricted our study to a modal theory. This approach is limited in two ways. First, it does not allow description of perturbations which are localized in space, and secondly, it does not account for transient effects. The first direction was explored by Fabre (2002) through a computation of the linear initial value problem. This study shows that generally, part of the energy propagates along the vortex in the form of wave packets, while another part of the energy is rapidly dissipated through a filamentation of vorticity. The second direction was investigated by Antkowiak & Brancher (2004) using an optimal perturbation analysis. This study shows that very large transient amplifications can be reached for perturbations initially located outside the vortex core. The present cartography of eigenmodes gives hints on how to interpret the results of both studies.

Third, the study was restricted to the discrete eigenmodes. However, these discrete eigenmodes do not form a complete basis to represent an arbitrary perturbation. Another class of modes, called continuum modes, has to be included. The existence of these modes, which form the continuous spectrum of the vortex, was only briefly evoked. The mathematical description of this continuous spectrum remains an open issue (see Appendix A) and its physical significance also remains to be studied. It may play a fundamental role in the transient behaviour of vortices.

Finally, the effect of nonlinearities on Kelvin waves remains an open question. This point is particularly interesting for the case of critical layer waves. In the case of parallel flows, it is known that nonlinear effects within a critical layer can completely change the properties of the waves, and lead to the formation of undamped, nonlinear waves. Le Dizès (2000) recently used this idea to construct nonlinear oscillation modes of a two-dimensional vortex, which take the form of tripolar vortices. The extension of this idea to the three-dimensional case is challenging. It may lead to the discovery of a new family of non-damped nonlinear retrograde waves.

This work was partially supported by the project "FAR-Wake" financed by the European Community under grant AST4-CT-2005-012338.

Appendix A. The continuous spectrum

The objective of this paper is to describe the Kelvin waves, which form the *discrete spectrum* of a vortex. However the existence of a *continuous spectrum* was briefly evoked in § 4, and its location in the complex ω-plane was described in figure 7. This continuous spectrum is the equivalent of the one initially described by Grosch & Salwen (1978) in unbounded viscous shear flows. In this Appendix we briefly discuss the significance of this continuous spectrum, and give an argument indicating that it is located along the negative imaginary axis in the complex ω-plane.

The values of ω in the continuous spectrum do not correspond to regular eigenmodes. However, they can be associated with a class of generalized eigenmodes, which are solutions of the stability equations in a weak sense: they satisfy the differential equations and the limit conditions, but they are not square-integrable. They are not acceptable as solutions to the stability problem when considered individually, and only an integral collection of these can be given a physical sense.

Such generalized eigenmodes may be constructed by solving the stability equations as a shooting problem, just as in the pioneering study of Lessen & Paillet (1974). The viscous equations being of order six, six independent solutions can be constructed and have to be matched with the imposition of limit conditions. When considering the asymptotic behaviour as $r \to \infty$, it is found that these independent solutions behave respectively as $r^{-1/2}\mathrm{e}^{kr}$, $r^{-1/2}\mathrm{e}^{-kr}$, $r^{-1/2}\mathrm{e}^{\beta r}$ (twice) and $r^{-1/2}\mathrm{e}^{-\beta r}$ (twice), with $\beta^2 = k^2 - \mathrm{i}\omega Re$ (Lessen & Paillet 1974). Among these solutions, three of them generally grow exponentially and have to be removed. This provides three conditions to be imposed on the eigensolutions. Three other conditions arising from the limit conditions at $r = 0$, one is led to a well-posed eigenvalue problem allowing computation of the discrete eigenmodes. However, a degeneracy occurs as soon as β^2 is real and negative. In this case, only one out of the six solutions grows exponentially and can be removed. Perturbations containing the five other solutions can always be constructed, and these perturbations turn out to be not square-integrable. This is precisely the expected behaviour for modes belonging to the continuous spectrum. Accordingly, the condition $\beta^2 < 0$ indicates a possible location of the continous spectum in the complex ω-plane: $\omega_r = 0$, $\omega_i < -k^2/Re$.

The argument presented here should, however, be considered as preliminary. Clearly additional work is required to describe more precisely this continuous spectrum, and to investigate its contribution to the dynamics of the vortex.

Appendix B. The complex mapping function

When using a complex collocation method, the stability equations are not directly solved in terms of the physical variable r, but are first mapped to a reduced variable $\xi \in [-1, 1]$ through a mapping function. The choice of the mapping function is crucial for the performance of the method, and different functions have been proposed and discussed (Canuto *et al.* 1988; Khorrami, Malik & Ash 1989).

Here, two mapping functions have been used. The first one is the algebraic mapping introduced by Fabre & Jacquin (2004*b*):

$$r = \frac{H\xi}{1 - \xi^2}. \tag{B 1}$$

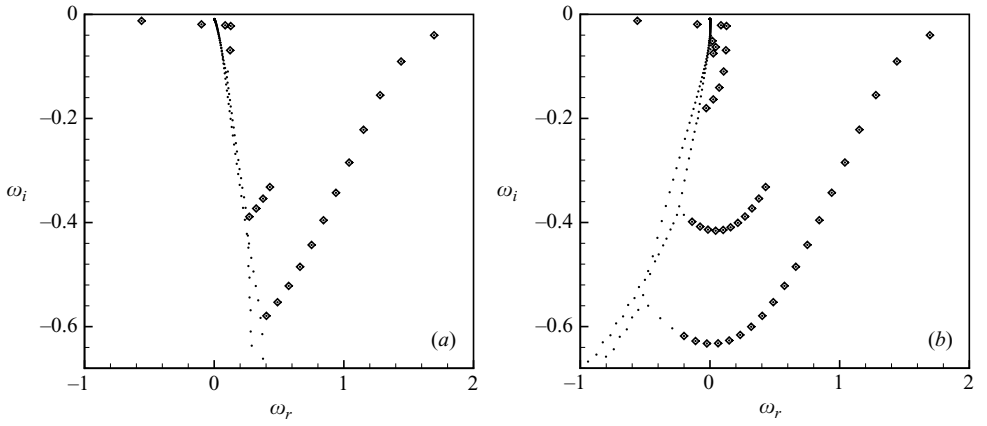

FIGURE 25. Numerical spectrum in the complex ω-plane for $m = 1$, $k = 3$, $Re = 1000$, computed using (*a*) a real mapping function, and (*b*) a complex mapping function. The diamond symbols and the dots indicate, respectively, the converged and spurious eigenmodes.

This function depends upon a single parameter H which controls the spreading of the collocation points. The second one is a complex mapping, defined as follows:

$$r = \frac{H\xi}{1-\xi^2} + \mathrm{i}\frac{A\xi}{\sqrt{1-\xi^2}}, \tag{B 2}$$

with $H = 2.217792$, $A = 2.139777$.

Other choices of function could have been used, and several were tested. The mapping function given by equation (B 2) proved to be the most successful, and some of the reasons for this success will be explained below.

Let us compare the efficiency of these mappings, for the choice of parameters $m = 1$, $k = 3$, $Re = 1000$. This case has already been considered in § 5, and the corresponding theoretical spectrum has been displayed in figure 7. As recalled in Appendix A, the theoretical spectrum contains both a set of discrete eigenvalues, which correspond to the Kelvin waves, and a continuous spectrum, which takes the form of a branch cut located along the imaginary axis.

Figure 25(*a*) displays the spectrum computed with the real mapping (B 1). This numerical spectrum contains both physical and spurious eigenvalues. The physical eigenvalues, displayed by diamond symbols do not depend upon the discretization parameters, and are sorted using a suitably defined convergence criterion (see Fabre & Jacquin 2004*b*). The spurious eigenvalues, displayed by dots, form a 'curtain' which roughly occupies the position of the continuous spectrum. (The same phenomenon occurs in the eigenspectra of plane shear flow; see Schmid & Henningson 2002, p. 67.) When comparing this spectrum with the exact result, it is found that the eigenvalues corresponding to the C, V and D families are correctly resolved. On the other hand, only four eigenvalues of the L family can be computed efficiently. The other expected eigenvalues are somehow hidden behind the 'curtain' of spurious eigenvalues. Increasing the number of collocation points slightly displaces the 'curtain' and reveals a few additional eigenvalues. However, when using a real mapping, the problem can never be completely fixed.

Figure 25(*b*) displays the same spectrum computed with the complex mapping (B 2). The change is spectacular: the 'curtain' of spurious eigenmodes is displaced to the

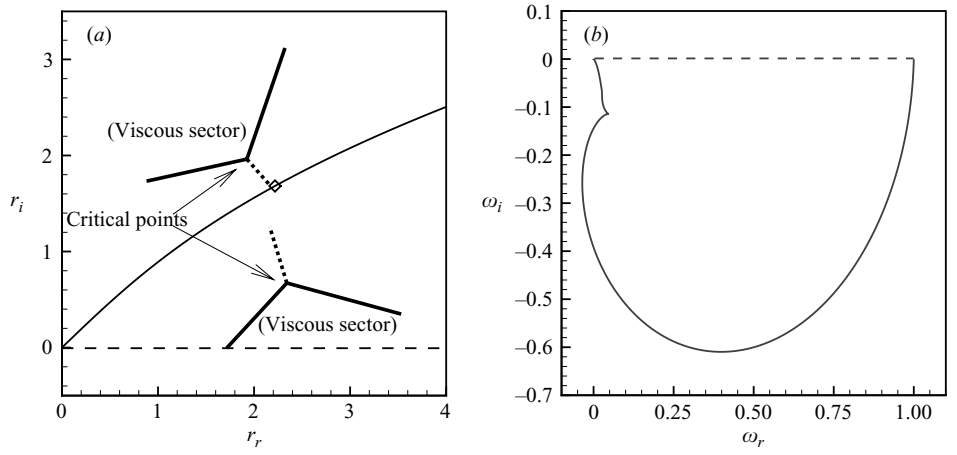

FIGURE 26. (*a*) "Integration paths" in the complex r-plane, corresponding to the complex mapping function (B 2) (full line) and to the real mapping function (B 1) (dashed line). The thick lines represent the Stokes lines bounding the viscous sectors (for a particular mode defined in the text), and the diamond symbol corresponds to the point $r = 2.2178 + 1.6822\mathrm{i}$. (*b*) Traces in the complex ω-plane of the complex mapping function (B 2) (full line) and of the real mapping function (dashed line).

left, with the effect to 'uncover' new eigenvalues which were hidden behind it. At least seven eigenvalues of each of the L, V and C families are thus discovered.

Note, however, that among the newly uncovered modes, we have only retained those located in right half of the complex plane $\omega_r > 0$. In effect, the continuous spectrum, which we assume to lie along the imaginary axis, introduces a cut in the complex plane, and we cannot assess whether modes located at the left side of this cut belong to the 'good sheet' of the complex plane or not. (Anyway, these discarded modes are always substantially damped.)

Let us now explain briefly how the complex mapping works. A mapping can be thought of as an 'integration path' in the complex r-plane where the differential equations of the stability problem are solved. Figure 26(*a*) displays, in the complex r-plane, the integration paths of our real and complex mappings, as well as the typical structure of an L-mode. The chosen mode is the one depicted in figure 14(*d*): $k = 0.5$, $\omega = 0.1439 - 0.0900\mathrm{i}$. The corresponding two first critical points are given by Sipp & Jacquin (2003), and the Stokes lines are drawn according to Le Dizès (2004). The integration path of the real mapping (dashed line) lies on the real axis, and intersects the lowest viscous sector of the mode. On the other hand, the integration path of the complex mapping correctly passes between the viscous sectors. The mapping function was designed, precisely, to avoid the viscous sectors of most of the L modes. In particular, the constants H and A of the mapping were carefully set in order for the path to pass through the point $r = 2.2178 + 1.6822\mathrm{i}$, corresponding to the diamond symbol in the figure, which is always located between the viscous sectors (see Sipp & Jacquin 2003, and Appendix C).

The performance of a mapping can also be understood when considering its 'trace' in the complex ω-plane, which is the image of the integration path through the function $\omega = m\Omega(r)$. In effect, it can be shown that a necessary condition for the integration path to pass above the lower critical point of a particular mode is for its trace in the complex ω-plane to pass below the frequency of this mode.

The traces of both the real and the complex mappings are displayed in figure 26(*b*) (for $m = 1$). The trace of the real mapping (dashed line) is the real segment $\omega \in [0, 1]$. Therefore it is not surprising that this mapping is unable to resolve most of the L eigenmodes which are located below it. On the other hand, the trace of the complex mapping (full line) passes well below the region containing all the eigenvalues, and is therefore an efficient way to compute them.

Finally, we have to explain the very unusual behaviour of our complex mapping at $\xi \to \pm 1$. Normally, one would expect the mapping function to come back to the real r-axis, because the boundary conditions are to be imposed at $r = \pm\infty$ in the real direction. But, for the mapping (B 2), the imaginary part of r diverges at $\xi \to \pm 1$. However, r_i grows less rapidly than r_r, so that the path actually tends to the direction of the real axis in a kind of "parabolic" way. This point may seem quite tricky, but it was the only way for the trace of the mapping in the complex ω-plane to come back to $\omega = 0$ 'from below', and therefore to achieve the best resolution.

Appendix C. The inviscid singular modes (Landau poles)

In this Appendix we present results obtained for inviscid singular modes, for $m = 1$ and $m = 2$. The numerical method used for this purpose is a shooting method closely related to that used by Sipp (1999) and Sipp & Jacquin (2003). A contour deformation rule has also been applied here, but in a different way than for the viscous case. As explained in Sipp & Jacquin (2003), the inviscid equations are singular at the critical points r_c, which precisely correspond to the turning points of the viscous equations, defined by (5.1). This relation defines a multi-valuated complex function $r_c(\omega)$ related to the complex Lambert function. So for each value of ω there is an infinite number of critical points r_c. As stated by Sipp & Jacquin (2003), and justified by Le Dizès & Lacaze (2005), the integration path has to pass above the critical point of order zero (corresponding to the principal branch of the Lambert function), and below the critical points of higher order. In practice, the first four critical points were tracked and the integration path was continuously deformed as the branches were computed. Note that the spectral collocation method used in the viscous case has also been applied here, and an excellent agreement was obtained between both methods. However, the shooting method was found to be the most efficient to track the branches down to $k = 0$.

Figure 27 displays the frequencies (real and imaginary parts) computed for $m = 1$. Three families of branches are displayed, and are referred to as inviscid singular modes of the first, second and third kind. The first ones, displayed with thick lines, were described by Sipp & Jacquin (2003). The two other kinds are newly discovered. The figure displays six branches of the first kind, nine of the second kind and two of the third kind, but it is likely that an infinite series exists for each kind. Contrary to the first kind of branch which becomes neutral above a given value of their wavenumber k, the new branches remain damped for all k. Note, however, that for moderate values of k they are relatively less damped than those of the first kind.

Sipp & Jacquin (2003) carefully analysed the behaviour of the first kind of branch as $k \to 0$. They showed that the frequencies of all branches tend to a common limit. Moreover, they showed that in that limit the critical points of order zero and one coincide (see figure 12 of Sipp & Jacquin 2003). The same phenomenon was found to occur for the second and third kind of branches. However, for the second kinds of branch the coincidence occurs between the critical points of order zero and two, and for the third kind between the critical points of order zero and three. This property

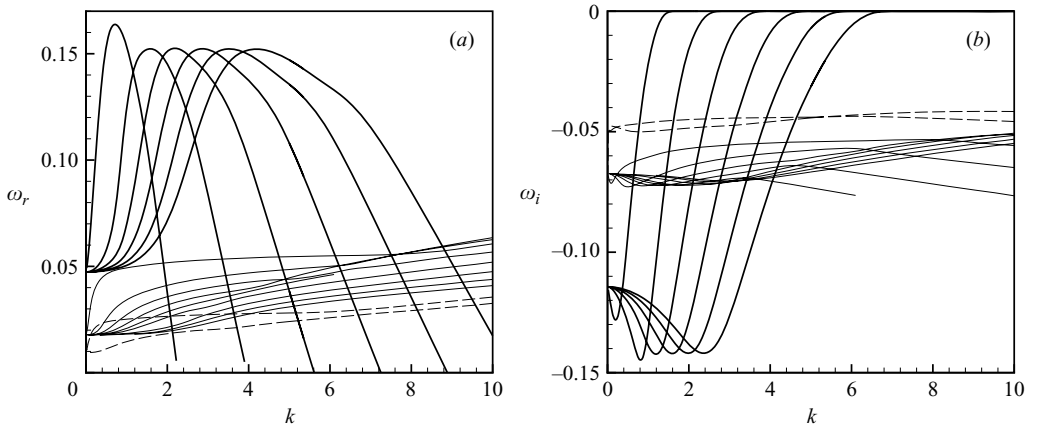

FIGURE 27. Frequencies of the inviscid singular modes for $m = 1$: (a) oscillation rates ω_r, (b) damping rates ω_i. Thick lines, thin lines and dashed lines correspond, respectively, to inviscid singular modes of the first kind, second, and third kind.

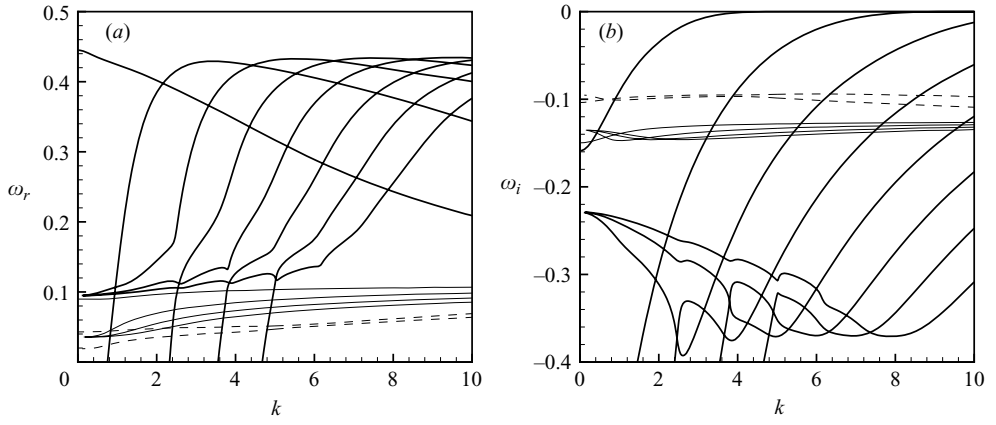

FIGURE 28. Frequencies of the inviscid singular modes for $m = 2$. Same legend as in figure 27.

served as a guideline in the discovery of these new families of branches. We have not considered the possibility of a coincidence with the critical points of order four, five, etc., but it is very likely that each of the critical points will lead to a new set of branches.

Note that a coincidence between two critical points at a location r_0 necessarily corresponds to a root of the equation $\Omega'(r_0) = 0$. This property may be used to predict the $k = 0$ limit of the branches. The first root of this equation is $r_0 = 2.2178 + 1.6822\mathrm{i}$, and gives the limit frequency for the first kind of branch: $\omega = 0.04746 - 0.1144\mathrm{i}$. The two next roots are $r_0 = 2.8979 + 2.3946\mathrm{i}$ and $r_0 = 3.4260 + 2.9515\mathrm{i}$ and give the limit frequencies for the second and third kinds of branch, respectively: $\omega = 0.01778 - 0.06736\mathrm{i}$, and $\omega = 0.009469 - 0.04756\mathrm{i}$.

Finally, figure 28 displays the frequencies (real and imaginary parts) computed for $m = 2$ in the same way. Here again, branches belonging to the first, second and third kinds could be computed. The first kind of branch was described by Sipp & Jacquin (2003). The behaviour of these branches is much more complicated than for $m = 1$, but was partially explained by the asymptotic analysis of Le Dizès & Lacaze (2005).

The new kinds of branch seem, comparatively, more regular. Note that as $k = 0$, all branches of the same kind do not necessarily have the same limit, although a fraction of these do.

REFERENCES

Antkowiak, A. & Brancher, P. 2004 Transient energy growth for the Lamb-Oseen vortex. *Phys. Fluids* **16**, L1–L4.

Arendt, S., Fritts, D. C. & Andreassen, O. 1997 The initial value problem for Kelvin vortex waves. *J. Fluid Mech.* **344**, 181–212.

Ash, R. L. & Khorrami, M. R. 1995 Vortex stability. In *Fluid Vortices* (ed. S. I. Green), chap. 8, pp. 317–372. Kluwer.

Barenghi, C. F., Donelli, R. & Wien, W. F. 2001 *Quantized Vortex Dynamics and Superfluid Turbulence*. Lecture Notes in Physics, vol. 571. Springer.

Benjamin, T. B. 1962 Theory of the vortex breakdown phenomenon. *J. Fluid Mech.* **14**, 593–629.

Bernoff, A. J. & Lingevitch, J. F. 1994 Rapid relaxation of an axisymmetric vortex. *Phys. Fluids* **6**, 3717–3723.

Briggs, R. J., Daugherty, J. D. & Levy, R. H. 1970 Role of Landau damping in crossed-field electron beams and inviscid shear flows. *Phys. Fluids* **13**, 421–432.

Canuto, C., Hussaini, Y. M., Quarteroni, A. & Zang, T. A. 1988 *Spectral Methods in Fluid Dynamics*. Springer.

Crouch, J. D. 1997 Instability and transient growth for two trailing-vortex pairs. *J. Fluid Mech.* **350**, 311–330.

Crow, S. 1970 Stability theory for a pair of trailing vortices. *AIAA J.* **8**, 2172–2179.

Drazin, P. & Reid, W. 1981 *Hydrodynamic Stability*. Cambridge University Press.

Eloy, C. & Le Dizès, S. 2001 Stability of the Rankine vortex in a multipolar strain field. *Phys. Fluids* **13**, 660–676.

Fabre, D. 2002 Instabilités et instationnarités dans les tourbillons: Application aux sillages d'avions. PhD thesis, Université Paris VI (availible at http://www.site.voila.fr/erbaf).

Fabre, D. & Jacquin, L. 2004*a* Short-wave cooperative instabilities in representative aircraft vortices. *Phys. Fluids* **16**, 1366–1378.

Fabre, D. & Jacquin, L. 2004*b* Viscous instabilities in trailing vortices at large swirl number. *J. Fluid Mech.* **500**, 239–262.

Fabre, D., Jacquin, L. & Loof, A. 2002 Optimal perturbations in a four-vortex aircraft wake in counter-rotating configuration. *J. Fluid Mech.* **451**, 319–328.

Fabre, D. & Le Dizès, S. 2006 Viscous and inviscid centre-modes in vortices: the vicinity of the neutral curves. In preparation.

Fritts, D. C., Arendt, S. & Andreassen, O. 1998 Vorticity dynamics in a breaking internal gravity wave. Part 2. Vortex interactions and transition to turbulence. *J. Fluid Mech.* **367**, 47–65.

Fukumoto, Y. 2003 The three-dimensional instability of a straight vortex filament revisited. *J. Fluid Mech.* **493**, 287–318.

Grosch, C. & Salwen, H. 1978 The continuous spectrum of the Orr-Sommerfeld equation. Part 1. The spectrum and the eigenfunctions. *J. Fluid Mech.* **87**, 33–54.

Hopfinger, E. J., Browand, F. K. & Gagne, Y. 1982 Turbulence and waves in rotating tank. *J. Fluid Mech.* **125**, 505–534.

Jacquin, L., Fabre, D., Sipp, D., Theofilis, V. & Vollmers, H. 2003 Instability and unsteadiness of wake vortices. *Aero. Sci. Tech.* **7**, 577–593.

Kelvin, Lord 1867 On vortex atoms. *Proc. R. Soc. Edinburgh* **VI**, 94–105, reprinted in *Phil. Mag.* **XXXIV**, 15–24.

Kelvin, Lord 1880 Vibrations of a columnar vortex. *Phil. Mag.* **10**, 155–168.

Kerswell, R. R. 2002 Elliptical instability. *Annu. Rev. Fluid Mech.* **34**, 83–113.

Khorrami, M. R., Malik, M. R. & Ash, R. L. 1989 Application of spectral collocation techniques to the stability of swirling flows. *J. Comput. Phys.* **81**, 206–229.

Klein, R. & Majda, A. J. 1991*a* Self-stretching of a perturbed vortex filament. I. The asymptotic equation for deviations from a straight line. *Physica*D **49**, 323–352.

Klein, R. & Majda, A. J. 1991*b* Self-stretching of a perturbed vortex filament. II. Structure of solutions. *Physica D* **53**, 267–294.

Le Dizès, S. 2000 Non-axisymmetric vortices in two-dimensional flows. *J. FLuid Mech.* **406**, 175–198.

Le Dizès, S. 2004 Viscous critical layer analysis of vortex normal modes. *Stud. Appl. Maths* **112**, 315–332.

Le Dizès, S. & Fabre, D. 2006 Large-Reynolds-number asymptotic analysis of viscous centre-modes in vortices. In preparation.

Le Dizès, S. & Lacaze, L. 2004 An asymptotic description of vortex Kelvin modes. *J. Fluid Mech.* **542**, 69–96.

Le Dizès, S. & Laporte, F. 2002 Theoretical predictions for the elliptic instability in a two-vortex flow. *J. Fluid Mech* **471**, 169–201.

Leibovich, S. 1970 Weakly non-linear waves in rotating fluids. *J. Fluid Mech.* **42**, 803–822.

Leibovich, S., Brown, S. & Patel, Y. 1986 Bending waves on inviscid columnar vortices. *J. Fluid Mech.* **173**, 595–624.

Lessen, M. & Paillet, F. 1974 The stability of a trailing line vortex. Part 2. Viscous theory. *J. Fluid Mech.* **65**, 769–79.

Lin, C. 1955 *The Theory of Hydrodynamic Stability*. Cambridge University Press.

Mayer, E. W. & Powell, K. G. 1992 Viscous and inviscid instabilities of a trailing vortex. *J. Fluid Mech.* **245**, 91–114.

Melander, M. V. & Hussain, F. 1993 Coupling between a coherent structure and fine-scale turbulence. *Phys. Rev.* E **48**, 2669–2689.

Melander, M. V. & Hussain, F. 1994 Core dynamics on a vortex column. *Fluid Dyn. Res.* **13**, 1–37.

Miyazaki, T. & Hunt, J. C. R. 2000 Linear and nonlinear interactions between a columnar vortex and external turbulence. *J. Fluid Mech.* **402**, 349–378.

Moet, H., Laporte, F., Chevalier, G. & Poinsot, T. 2005 Wave propagation in vortices and vortex bursting. *Phys. Fluids* **17**, 054109.

Moore, D. W. & Saffman, P. G. 1972 Motion of a vortex filament with axial flow. *Proc. R. Soc. Lond.* A **292**, 407–429.

Moore, D. W. & Saffman, P. G. 1975 The instability of a straight vortex filament in a strain field. *Proc. R. Soc. Lond.* A **346**, 413–425.

Rossi, M. 2000 Of vortices and vortical layers: An overview. In *Vortex Structure and Dynamics* (ed. A. Maurel & P. Petitjeans). Lecture Notes in Physics, vol. 555, pp. 40–123. Springer.

Rutherford, E. 1911 The scattering of α and β rays and the structure of the atom. *Proc. Manchester Lit. Phil. Soc.* **IV** (55), 18–20.

Saffman, P. 1992 *Vortex Dynamics*. Cambridge University Press.

Samuels, D. C. & Donnelly, R. J. 1990 Sideband instability and recurrence of Kelvin waves on vortex cores. *Phys. Rev. Lett.* **64**, 1385–1388.

Schecter, D. A., Durbin, D. H. E., Cass, A. C., Dritscoll, C. F., Lansky, I. M. & O'Neil, T. M. 2000 Inviscid damping of asymmetries on a two-dimensional vortex. *Phys. Fluids* **12**, 2397–2412.

Schmid, P. J. & Henningson, D. S. 2001 *Stability and Transition in Shear Flows.* Applied Mathematical Sciences, Vol. 142. Springer.

Sipp, D. 1999 Instabilités dans les écoulements tourbillonnaires. PhD thesis, École polytechnique, Palaiseau, France.

Sipp, D. & Jacquin, L. 2003 Widnall instabilities in vortex pairs. *Phys. Fluids* **15**, 1861–1874.

Spalart, P. 1998 Airplane trailing vortices. *Annu. Rev. Fluid Mech.* **30**, 107–138.

Tsai, C.-Y. & Widnall, S. E. 1976 The stability of short waves on a straight vortex filament in a weak externally imposed strain field. *J. Fluid Mech.* **73**, 721–733.

Widnall, S. E., Bliss, D. & Zalay, A. 1971 Theoretical and experimental study of the stability of a vortex pair. In *Aircraft Wake Turbulence* (ed. R. M. Olsen, A. Goldburg & J. B. Rodgers). Plenum.